mathematics

IMPACT FACTOR 2.2

CITESCORE 4.6

Article

Quantum Entanglement Between Charge Qubit and Mechanical Cat-States in Nanoelectromechanical System

Matija Tečer and Danko Radić

MDPI

https://doi.org/10.3390/math13132054

mathematics

MDPI

Article

Quantum Entanglement Between Charge Qubit and Mechanical Cat-States in Nanoelectromechanical System

Matija Tečer [1,2] and Danko Radić [1,*]

[1] Department of Physics, University of Zagreb Faculty of Science, Bijenička 32, 10000 Zagreb, Croatia
[2] Dipartimento di Fisica e Astronomia "G. Galilei", University of Padua, Via Marzolo 8, I-35131 Padova, Italy
* Correspondence: dradic@phy.hr

Abstract

We present a detailed mathematical description, both an analytical model and a numerical simulation, of a physical system based on a superconducting nanoelectromechanical setup that generates nanomechanical cat-states entangled with charge qubit states. The system consists of a superconducting grain in a regime of the Cooper pair box (the charge qubit) that performs mechanical vibrations between two bulk superconductors. Operation of the device is based on the AC Josephson effect, i.e., the phase difference between superconducting electrodes is controlled by a DC bias voltage following the operational switch on/off protocol. We compare an analytical idealised solution with numerical simulation using experimentally feasible parameters, different decoherence processes, as well as imperfections of experimental procedures such as time-control of the bias voltage, to get insight into how they influence the time-evolution of the realistic system, deteriorate the quantum coherence, and affect the formation of the cat-states.

Keywords: nanoelectromechanical systems; AC Josephson effect; cat-states; quantum entanglement

MSC: 81V99

check for updates

Academic Editor: Paolo Crippa

Received: 24 May 2025
Revised: 15 June 2025
Accepted: 17 June 2025
Published: 20 June 2025

Citation: Tečer, M.; Radić, D. Quantum Entanglement Between Charge Qubit and Mechanical Cat-States in Nanoelectromechanical System. *Mathematics* **2025**, *13*, 2054. https://doi.org/10.3390/math13132054

1. Introduction

Future quantum technologies, namely those involving processing of quantum information (QI), crucially depend on the possibility of its storing and transportation. In that sense, a reliable way of transduction of the QI between optical, electronic, or mechanical degrees of freedom inside hybrid quantum devices is essential. A qubit [1], being the basic container of the QI, is in essence, a quantum two-level system where the QI is stored in the quantum superposition of two states, i.e., in a quantum phase [2]. The physical implementation of a qubit covers a number of fields in physics, such as optics, atomic physics, or solid-state physics, as well as their combinations [3–7]. Although, within the solid state implementations, the so-called "flux qubit" [8] and transmon [9,10] designs appear the most promising due to their properties, in this paper we limit our consideration to the charge qubit, realised as a superconducting (SC) mesoscopic grain in the regime of the Cooper pair box (CPB) [11–14], embedded in a nanoelectromechanical system (NEMS). The good side of a charge qubit is that there is a possibility of manipulating its states due to strong Coulomb-based coupling, which can be controlled, but it also draws its most negative side—a great sensitivity to external perturbations and noise, leading to rather short coherence time [12]. On the other hand, the mechanical subsystem within NEMS,

based on nano-oscillators or especially on surface phonons, can provide quite a long coherence time due to amazingly high quality factors achievable today [15–17]. A good example is the recent experimental achievement of control and detection of individual zero- and one-phonon itinerant Fock states inside a mechanical surface resonator coupled to the superconducting qubit [18,19]. In addition to the single phonon states, the other way to utilise the mechanical degrees of freedom of a nano-oscillator is to build a mechanical coherent state. Mechanical coherent state is a quantum state constructed by summing up all states of a harmonic oscillator, weighted by the Poisson distribution, all sharing a common phase relation, thus yielding the minimal uncertainty and being the closest to classical vibrational mode, but still obeying quantum principles. Furthermore, to encode a QI into a mechanical subsystem, one needs two of its states isolated from others to a substantial degree. It turns out that the best candidates for such two states are two "opposite" mechanical coherent states in quantum superposition, built in a controlled way. Such a quantum object is called the Schrödinger cat-state (or just a "cat-state")—a quantum superposition of two practically classical states opposite in their nature (dead and living cat in his original suggestion in then thought experiment).

Concerning our previous work, in this paper we present a deeper analysis, based on numerical simulations, of several key steps affecting formation of the cat-states compared to the previously considered idealised case, such as the realistic model of applying the bias voltage, or off-resonance mismatch in Cooper pair tunnelling, showing the numerically calculated corresponding cat-states, as well as estimating margins of their usability for the aforementioned purposes. Cat-states have been widely used in the field of quantum optics and photonics so far [20–26], but they pave their way in the field of nano(electro)mechanics as well [27–30]. One way of implementation into NEMS was suggested earlier by Radić et al. [31], followed by the suggestion of the transduction process of QI from charge qubit into mechanical cat-state [32]. That design is based on the AC Josephson effect between a superconducting mesoscopic grain placed between two superconducting bulk electrodes biased by a constant voltage. The grain is capable of performing mechanical vibrations between electrodes, in turn providing the position-dependent tunnelling of Cooper pairs between them and the grain. For such a setup, starting from the ground state of a mechanical oscillator, a time-protocol of switching on and off the bias voltage is proposed in order to create a mechanical cat-state entangled with charge qubit states. Naturally, in such a setup, a coherent interplay of qubit states and nanomechanical excitations is of vital importance [33–35], while the entanglement as such presents a powerful tool to achieve not only the described functionality, but also in the field of quantum communication in general [36].

With respect to the previous work [31], this paper is focused on mathematical modelling and numerical simulations in order to address the influence of the main sources of decoherence in the system, such as phonon loss or qubit state flip, as well as experimentally more realistic operating protocols comparing to the ideal one used in an analytical approach, e.g., the bias voltage switch on/off procedure, which is not instantaneous as ideally supposed. We aim to find conditions under which the cat-states can be achieved to a satisfactory degree. In that respect, we also give an estimation of the operational range of physical parameters required for the effect to take place, for which we find of vital importance the mechanical resonator frequency of the order of 1 GHz (and then using higher mode to elevate it by an order of magnitude), the 10 μeV bias voltage controlled to 0.1% precision achievable by modern equipment, and quality factor of mechanical resonator of at least 10^4, also perfectly within the reach of current techniques.

The paper is organised as follows: After this introduction, in Section 2, we present a schematic description of the proposed NEMS setup and introduce the Hamiltonian and

parameters. Section 3 presents an approximate analytical solution of the problem, leading to the formation of the cat-states, in order to shed light on the processes leading to it. In Section 4, we present an exact solution of the problem through extensive numerical simulations leading to the cat-states formation using physically realistic parameters, addressing the main effects that put the physical feasibility of the proposed model. Section 5 is a conclusion, followed by Appendix A, in which we explain some calculation details.

2. Description of the SC NEMS Setup

We consider a NEMS, schematically shown in Figure 1. The system is composed of a superconducting grain that oscillates between two bulk superconductors so that its mechanical degrees of freedom (DOFs) are described as a harmonic oscillator. The gate electrode controls the electrostatic energy of the grain by the potential V_G. By choosing a specific gate voltage, it is possible to bring the quantum state of the grain with n and the state with $n+1$ Cooper pairs into degeneracy (n is an integer number), i.e., to achieve that the electrostatic DOF of the grain operates as a CPB—a qubit in its essence. Quantum state $|0\rangle$ describes the state of the grain with n Cooper pairs, and state $|1\rangle$ the one with $n+1$ Cooper pairs. As we work in the charge qubit regime, Josephson's energy E_J is much smaller than the charging energy of the superconducting grain $E_c = e^2/2C$, where e is the electron charge and C is the electrical capacity of the grain. The grain performs mechanical oscillatory motion between the superconducting electrodes. Cooper pairs can tunnel from the grain to the electrodes and back [37,38]. Tunnelling induces a transition between the qubit states, with an amplitude that depends on the distance of the grain from the electrodes as well as on the superconducting phase difference between the two bulk superconductors (electrodes). That phase difference is controlled by the bias voltage V, with that being in our hands to be controlled externally. By controlling it, we can control the time evolution of the system. Since the tunnelling amplitude depends on the position of the grain, this tunnelling effect couples mechanical and qubit DOFs of the grain.

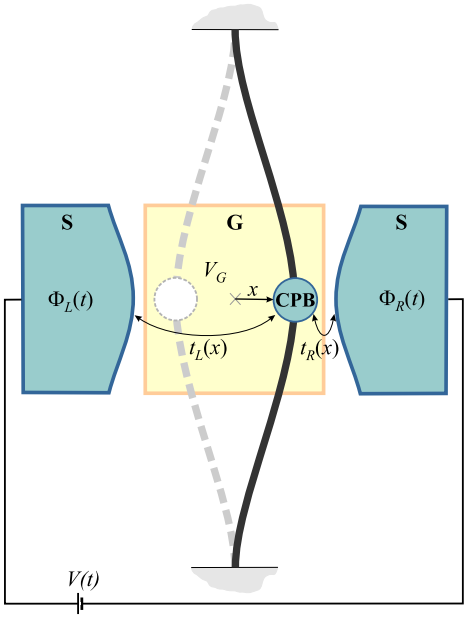

Figure 1. The system schematics: A superconducting mesoscopic grain (CPB), attached to an elastic beam or pillar, harmonically oscillates between two bulk superconductors (S) biased by voltage $V(t)$, which controls their relative phase $\phi = \Phi_R - \Phi_L$. Cooper pairs tunnel between S-electrodes and the CPB with position-dependent amplitudes $t_L(x)$ and $t_R(x)$, for "left" or "right" lead, determined by position x of the grain. Gate (G) controls the electrostatic energy of the grain via applied voltage V_G.

Hamiltonian $\hat{H}$ of the system under consideration can be written as [31]

$$\begin{aligned} \hat{H} &= \hat{H}_0 + \hat{H}_I, \\ \hat{H}_0 &= \hbar\omega\left(\hat{a}^\dagger\hat{a} + \frac{1}{2}\right) - E_j\cos(\phi(t))\hat{\sigma}_x, \\ \hat{H}_I &= \epsilon E_J \sin(\phi(t))\hat{X}\hat{\sigma}_y. \end{aligned} \tag{1}$$

Here, Hamiltonian $\hat{H}_0$ describes decoupled mechanical and qubit DOFs of the grain: ω is the frequency of mechanical harmonic oscillator (HO) corresponding to the period of oscillations $T = 2\pi/\omega$, E_J is the Josephson's energy, $\phi(t)$ is te time-dependent phase difference between the SC electrodes, and $a^\dagger$, a are creation and annihilation operators of mechanical bosonic excitations (phonons), operating in the mechanical subspace of the Hilbert space. Operators $\hat{\sigma}_i$, $i = x, y, z$ are Pauli matrices written in the basis where states $(0, 1)$ and $(1, 0)$ represent charged state with n and $n + 1$ Cooper pairs on the grain, respectively, i.e., they operate in the qubit (charge) subspace of the Hilbert space. Hamiltonian $\hat{H}_I$ describes the interaction between mechanical and qubit subsystems; $\hat{X}$ is the position operator of the grain, rescaled by the zero-point motion of the HO, $x_0 = \sqrt{\hbar/m\omega}$, where m is the mass of the grain. We assume that the tunnelling length $\lambda \gg x_0$ so that the interaction strength parameter $\epsilon \equiv x_0/\lambda \ll 1$. The dynamics of the system can be controlled by controlling the superconducting phase difference between the electrodes $\phi(t)$, which in turn can be controlled via the bias voltage $V(t)$, i.e.,

$$\frac{\partial\phi}{\partial t} = \frac{2eV(t)}{\hbar}. \tag{2}$$

By defining the time-protocol of manipulation with the bias voltage, we can control the time-evolution of the system to the desired state.

3. Approximative Analytical Solution

The analytical solution, although approximate, is developed in order to shed light and better understanding of the nature of processes and details related to the formation of the cat-states. We aim to consider a dynamical time-protocol for generating mechanical cat-states entangled to the charge qubit states. In this protocol, the bias voltage, initially zero, is turned on to the constant value V_0 at $t = 0$, and then we reverse its polarity to $-V_0$ at the specific time instant $t = t_1$, i.e.,

$$V(t) = \begin{cases} 0, & t < 0 \\ V_0, & t \in [0, t_1] \\ -V_0, & t > t_1 \end{cases}. \tag{3}$$

According to Equation (2), the phase $\phi(t)$ will evolve as

$$\phi(t) = \begin{cases} -\phi_0, & t < 0 \\ -\phi_0 + \Omega_J t, & t \in [0, t_1] \\ -\phi_0 + \Omega_J t_1 - \Omega_J(t - t_1), & t > t_1 \end{cases} \tag{4}$$

where ϕ_0 is some initial phase difference, and $\Omega_J \equiv 2eV_0/\hbar$ is the Josephson's frequency. In this consideration, we assume that the mechanical frequency is in resonance with the Josephson's frequency, i.e., $\omega = l\Omega_J$, where l is a positive integer.

We find the time-evolution operator of the system using the standard procedure within the interaction picture, i.e.,

$$\hat{U}(t,t') = \hat{U}_0(t)\hat{U}_I(t,t')\hat{U}_0^\dagger(t'), \tag{5}$$

$$\hat{U}_0(t) = \exp\left(-\frac{i}{\hbar}\int_0^t \hat{H}_0(t')dt'\right), \tag{6}$$

$$i\hbar\frac{\partial\hat{U}_I(t,t')}{\partial t} = \hat{\tilde{H}}_I(t)\hat{U}_I(t,t'). \tag{7}$$

where $\hat{U}(t,t')$ is the total evolution operator in the Schrödinger picture, while $\hat{U}_I(t,t')$ is the evolution operator that describes time-evolution according to the interaction Hamiltonian $\hat{\tilde{H}}_I = \hat{U}_0^\dagger\hat{H}_I\hat{U}_0$ (interaction picture). To obtain $\hat{\tilde{H}}_I$, we first transform operators of mechanical and qubit subsystems accordingly by using Haddamard's lemma, commutation relations for bosonic operators $[\hat{a}^\dagger\hat{a},\hat{a}] = -\hat{a}$, $[\hat{a}^\dagger\hat{a},\hat{a}^\dagger] = \hat{a}^\dagger$, and Pauli matrices $[\hat{\sigma}_i,\hat{\sigma}_j] = 2i\epsilon_{ijk}\hat{\sigma}_k$, transforming $\hat{a}\to\hat{a}(t)$ and $\hat{\sigma}_y\to\hat{\sigma}_y(t)$, i.e.,

$$\begin{aligned} &e^{i\omega\hat{a}^\dagger\hat{a}\,t}(\hat{a}^\dagger+\hat{a})e^{-i\omega\hat{a}^\dagger\hat{a}\,t} = \hat{a}^\dagger e^{i\omega t} + \hat{a}e^{-i\omega t},\\ &e^{-i\frac{E_J}{\hbar\Omega_J}\xi(t)\hat{\sigma}_x}\hat{\sigma}_y e^{i\frac{E_J}{\hbar\Omega_J}\xi(t)\hat{\sigma}_x} = \hat{\sigma}_y\cos\left(\frac{2E_J}{\hbar\Omega_J}\xi(t)\right) + \hat{\sigma}_z\sin\left(\frac{2E_J}{\hbar\Omega_J}\xi(t)\right), \end{aligned} \tag{8}$$

where $\xi(t)\equiv\int_0^t\cos(\phi(t'))dt'$. Using the above operators, we obtain

$$\hat{\tilde{H}}_I = \epsilon E_J\Big[\big(g_1(t)\hat{X}+g_2(t)\hat{P}\big)\hat{\sigma}_y + \big(g_3(t)\hat{X}+g_4(t)\hat{P}\big)\hat{\sigma}_z\Big], \tag{9}$$

featuring position and momentum operators $\hat{X} = (\hat{a}^\dagger+\hat{a})/\sqrt{2}$ and $\hat{P} = i(\hat{a}^\dagger-\hat{a})/\sqrt{2}$ in mechanical space, operators $\hat{\sigma}_{y,z}$ in qubit space, and time-dependent factors $g_i(t)$. Functions $g_i(t)$, i.e.,

$$\begin{aligned} g_1(t) &= \cos\left(\frac{2E_J}{\hbar\Omega_J}\xi(t)\right)\sin(\phi(t))\cos(\omega t),\\ g_2(t) &= \cos\left(\frac{2E_J}{\hbar\Omega_J}\xi(t)\right)\sin(\phi(t))\sin(\omega t),\\ g_3(t) &= \sin\left(\frac{2E_J}{\hbar\Omega_J}\xi(t)\right)\sin(\phi(t))\cos(\omega t),\\ g_4(t) &= \sin\left(\frac{2E_J}{\hbar\Omega_J}\xi(t)\right)\sin(\phi(t))\sin(\omega t), \end{aligned} \tag{10}$$

implicitly depend on the bias voltage $V(t)$ through the phase difference $\phi(t)$. We obtain a wave function of the system in the interaction picture by evolving its initial state by the solution of Equation (7). The wave function in the interaction and Schrödinger pictures are related via $\hat{U}_0$: the wave function in the Schrödinger picture evolves the same way as the one in the interaction picture, but its mechanical and qubit DOFs additionally rotate in the phase space and on the Bloch sphere with frequencies ω and Ω_J, respectively.

Since Equation (7) cannot be solved exactly in an analytical manner, to obtain the analytical solution, we use the rotating wave approximation (RWA). In that sense, we expand the Hamiltonian in Equation (9) in a Fourier series and keep only the constant terms (stationary phase). In that way, we obtain the Schrödinger equation with the time-independent Hamiltonian, which can be easily integrated.

Performing analytical calculations, we find out that, in order to create symmetric cat-states (coherent states in superposition with coefficients of the same magnitude), the polarity of the bias voltage should be reversed at the specific instant of time t_1 determined by

$$\begin{aligned} A\sin(\phi_0) &= (2K+1)\tfrac{\pi}{2},\\ \Omega_J t_1 &= \arcsin\Big(\Big(M-\tfrac{2K+1}{2}\Big)\tfrac{\sin(\phi_0)}{2K+1}\Big)+\phi_0+R\pi,\quad M,K,R\in\mathbb{Z}, \end{aligned} \tag{11}$$

where $A \equiv 2E_J/\hbar\Omega_J$. Since Ω_J can be controlled by controlling the voltage magnitude V_0 and since we can choose when to reverse the polarity of the bias voltage, those two conditions can be fulfilled. These conditions are obtained by imposing that the mean values (zeroth Fourier coefficient) of functions $g_1(t)$ and $g_2(t)$ are zero for $t < t_1$, and the mean values of functions $g_3(t)$ and $g_4(t)$ are zero for $t > t_1$.

We assume that the initial state of a system is a product state $|\psi(t=0)\rangle = |+x\rangle \otimes |0\rangle$, with $|0\rangle$ being the ground state of the HO and $|\pm x\rangle$ being the eigenstate of $\hat{\sigma}_x$ matrix with a positive/negative eigenvalue for a qubit (analogously, $|\pm y\rangle$ and $|\pm z\rangle$ are eigenstates of $\hat{\sigma}_y$ and $\hat{\sigma}_z$). By using a set of parameters that satisfy Equation (11), we calculate the wave function in the interaction picture at a time t,

$$|\psi(t)\rangle = \frac{1}{\sqrt{2}}\Big(|+\rangle \otimes |\psi_+(t)\rangle + |-\rangle \otimes |\psi_-(t)\rangle\Big), \tag{12}$$

where time-independent qubit states are defined as

$$|\pm\rangle \equiv \begin{cases} |\pm z\rangle, & t < t_1 \\ |\pm y\rangle, & t > t_1, \end{cases} \tag{13}$$

and time-dependent mechanical states as

$$|\psi_+\rangle \equiv \begin{cases} |-\alpha_1\rangle, & t < t_1 \\ \Big(\beta|-\alpha_1-\alpha_2\rangle - i\beta^*|\alpha_1-\alpha_2\rangle\Big), & t > t_1 \end{cases} \tag{14}$$

$$|\psi_-\rangle \equiv \begin{cases} |\alpha_1\rangle, & t < t_1 \\ \Big(\beta^*|-\alpha_1+\alpha_2\rangle + i\beta|\alpha_1+\alpha_2\rangle\Big), & t > t_1. \end{cases} \tag{15}$$

Here, states $|\alpha_1\rangle$ and $|\alpha_2\rangle$ represent nanomechanical coherent states of phonons, with time-dependent complex amplitudes α_1 and α_2, respectively, multiplied by factor $\beta \equiv \exp[i\,\mathrm{Im}(\alpha_2\alpha_1^*)]/\sqrt{2}$. Complex amplitude α_1 is linearly proportional to time t before the voltage flip, which can be tracked by studying the mean number of phonons in the mechanical subsystem, i.e.,

$$\langle\hat{N}(t)\rangle = \langle\hat{a}^\dagger\hat{a}\rangle = \mathrm{Tr}\big(\hat{\rho}_m\hat{N}\big) = |\alpha_1|^2 \propto t^2 \tag{16}$$

(see Figure 2), where $\hat{\rho}_m = \mathrm{Tr}_q(\hat{\rho})$ is the reduced density matrix of the mechanical subsystem obtained by tracing out qubit DOFs in the complete density matrix $\hat{\rho}(t) = |\psi(t)\rangle\langle\psi(t)|$. After the voltage polarity flip, one finds $\alpha_1 \propto t_1$ and $\alpha_2 \propto (t - t_1)$.

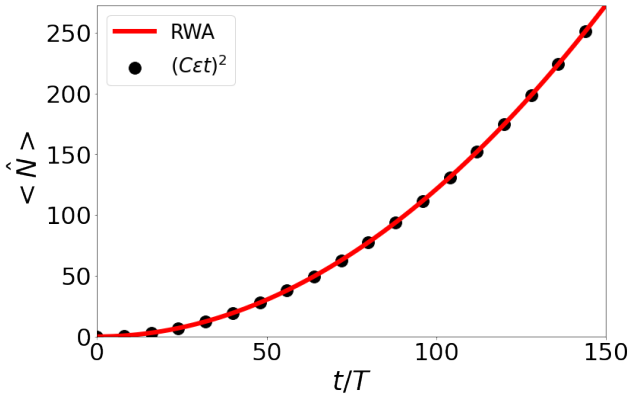

Figure 2. The mean number of phonons $\langle\hat{N}\rangle$ in time (scaled to period of mechanical vibrations T) is represented by the red solid curve for a protocol with constant bias voltage. Black dots represent the quadratic function $(C\epsilon t)^2$, where C is a constant that depends on system parameters, all obtained analytically within the RWA.

States of the mechanical subsystem $|\psi_{\pm}\rangle$, before the voltage flip at $t = t_1$, are coherent states entangled with qubit states as described by the wave function in Equation (12). After the flip, for time $t > t_1$, they become a superposition of two coherent states, by that constituting nanomechanical cat-states, entangled to qubit states. To confirm this, in Figure 3 we plot the Wigner function [39] of the mechanical subsystem,

$$W(x,p,t) = \frac{1}{\hbar\pi}\int \varrho(x+y,x-y,t)\exp\left(\frac{i}{\hbar}2py\right)\mathrm{d}y, \tag{17}$$

where $\varrho(x_1,x_2,t)$ is the density matrix of the mechanical subsystem described by $\hat{\rho}_m$ in $x-$representation, at times $t < t_1$ and $t > t_1$. For time $t < t_1$, $\hat{\rho}_m$ contains a mixture of two coherent states with the opposite amplitudes, while for $t > t_1$, $\hat{\rho}_m$ contains a mixture of two cat-states. Negative values of the Wigner function imply the non-classical nature of cat-states—a quantum superposition. From the previous discussion and Equations (14) and (15), it can be seen that the distance between coherent states, comprising a cat-state in the (X,P) phase space, is $2|\alpha_1| \propto t_1$, while the distance between the two cat-states that are entangled to different qubit states is $2|\alpha_2| \propto (t - t_1)$. Thus, by letting time t_1 be long enough, we can make each cat-state a superposition of two nearly orthogonal mesoscopic states.

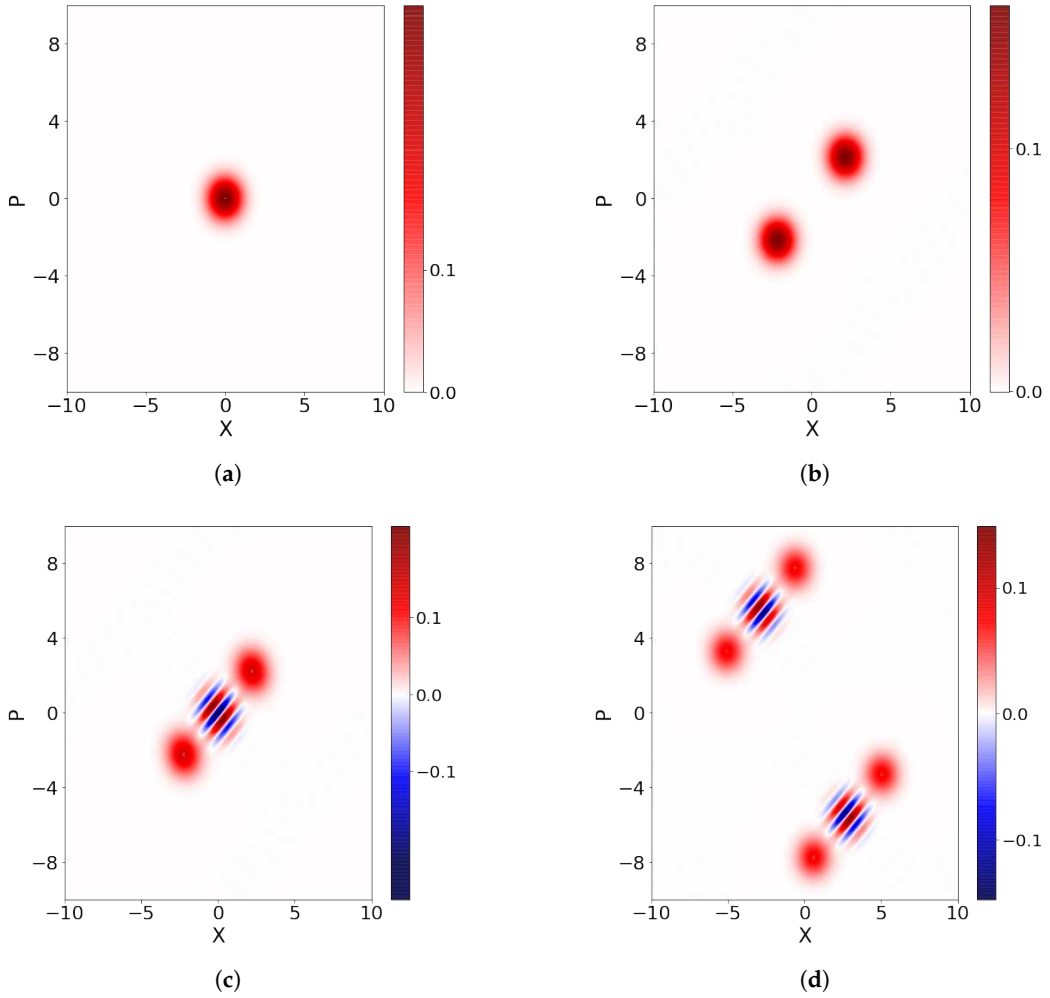

Figure 3. Time-evolution of the system from the initial state, creation of coherent states, forming and evolution of the cat-states. Density plot of the Wigner function of the mechanical subsystem (17) in the (X,P) phase space, for different times, using analytical RWA solution for the ideal time-protocol. (**a**) At $t = 0$, the ground state of the HO; (**b**) for $t < t_1$, a mixed state of two coherent states with opposite amplitudes; (**c**) for $t \approx t_1$, forming of the cat-states; (**d**) for $t > t_1$, a mixed state of two cat-states. The axes of the (X,P) space are in units of x_0 and $p_0 = \hbar/x_0$, respectively.

The "impurity" of the state described by ρ_m implies that the state of the whole qubit–resonator system is an entangled state. To quantify this entanglement, we plot entanglement entropy $S = \mathrm{Tr}_q(\hat{\rho}_q \ln \hat{\rho}_q)$, where $\hat{\rho}_q = \mathrm{Tr}_m(\hat{\rho})$, in Figure 4. Before the voltage polarity flip, entropy of entanglement increases monotonically, as the two coherent states, $\psi_+(t < t_1)$ and $\psi_-(t < t_1)$, become orthogonal to each other, and saturates to the value of maximally entangled state $S_{max} = \ln 2$. After the voltage polarity flip, $S(t)$ shows oscillatory features along the time interval of several periods T, and then again saturates the maximal value S_{max} as the cat-states $\psi_+(t > t_1)$ and $\psi_-(t > t_1)$ become orthogonal to each other.

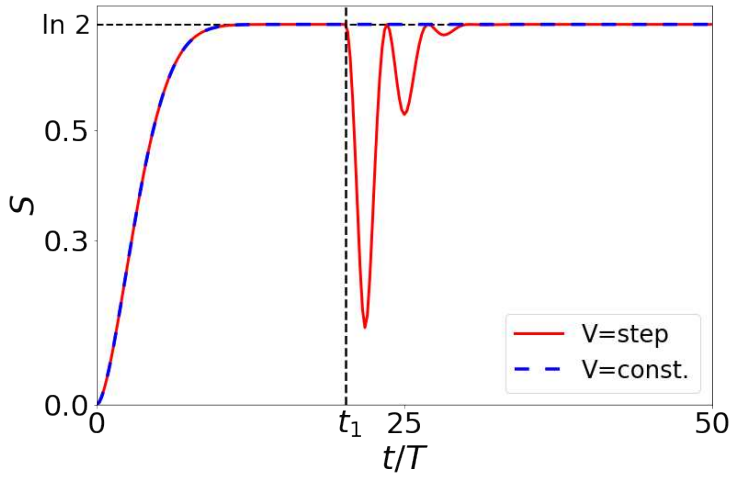

Figure 4. Entropy of entanglement S as a function of time (scaled to the period of mechanical oscillations T), obtained analytically within the RWA for different voltage protocols: (1) constant voltage V_0 for $t > 0$ (blue dashed curve); (2) voltage polarity change from V_0 to $-V_0$ at $t = t_1$ (red curve).

4. Numerical Simulations

In this section, we study the numerically obtained exact solution of the Schrödinger equation governed by the Hamiltonian (9). First we introduce values of the parameters that are used for numerical simulation, then we compare the RWA results with the exact numerical ones. After that, we do an extensive numerical analysis of the system by studying more realistic protocols, in the sense of experimental feasibility, than the one introduced in the previous section. Namely, we study what happens if conditions of resonance ($\omega = l\Omega_J$) and instantaneous voltage polarity flip exactly at the right moment are not strictly fulfilled. Later, we propose a more realistic voltage flip profile than the one in Equation (3) by introducing a hyperbolic tangent voltage profile instead of the step function. Finally, we introduce the phenomenological model of decoherence in the system and study the corresponding Lindbladian master equation.

4.1. Physical Parameters of the System

Numerical simulations were performed using the parameters that correspond to experimentally feasible values. We work in the charge-qubit regime for which the typical Josephson energy is $E_J \approx 10 \div 100\,\mu\mathrm{eV}$ (we use $E_J = 50\,\mu\mathrm{eV}$). To fulfil the symmetric cat-state formation condition (11), the Josephson frequency needs to be of the order of 10 GHz (we use $\Omega_J \approx 22.3\,\mathrm{GHz}$). To generate this kind of Josephson frequency, the bias voltage should be of the order of $10\,\mu\mathrm{V}$ (we use $V \approx 7.5\,\mu\mathrm{V}$). It can be controlled up to 0.1% precision [40]. For the resonance condition to be fulfilled, we need mechanical frequency of the same magnitude, i.e., $\omega = \Omega_J$ (we use frequency corresponding to period $T \approx 0.26\,\mathrm{ns}$), which is experimentally feasible utilizing, for example, the third bending mode of suspended carbon nanotube or some other setup [15,41–43] with typical

mass of attached superconducting grain of $10^{-22} \div 10^{-21}$ kg [41], which can still preserve superconductivity [44]. This combined with the mechanical frequency leads to $x_0 \approx 2 \div 6$ pm for the value of zero-point motion of the HO. For the typical tunnelling length $\lambda \approx 0.1$ nm, we obtain the the range of the small parameter $\epsilon \approx 0.01 \div 0.1$ (we use $\epsilon = 0.025$).

4.2. Validity of the RWA Approximation

The RWA is the widely used approximation in coupled resonant systems featuring the integrals with fast oscillating integrands, keeping the contributions with the stationary phase with the idea that the fast-oscillating terms (nonstationary, i.e., higher harmonics) will average out to zero if the coupling is weak enough and/or the time scale we study the effect is short enough. Those two criteria can be combined into one by defining the characteristic timescale up to which the RWA is valid. Beyond it, the higher harmonics (non-stationary terms) begin to build contributions that cannot be neglected. In that sense, the RWA should be valid as long as the interaction energy (coupling of qubit and mechanical resonator) $E_{int} = \epsilon E_J \sqrt{\langle X^2 \rangle} \propto \left(\epsilon E_J\right)^2 t/\hbar$ is small compared to the HO energy scale $\hbar\omega$, which is fulfilled for times $t < t_{RWA} = \left(\frac{\hbar}{\epsilon E_J}\right)^2 \omega$ [31]. To compare exact results to those obtained within the RWA, we calculate fidelity $F(t)$ of the RWA state $\psi_{RWA}(t)$, given by Equation (12), and the numerically obtained state $\psi(t)$,

$$F(t) = \left| \langle \psi_{RWA}(t) | \psi(t) \rangle \right|. \tag{18}$$

Corresponding infidelity, $1 - F(t)$, is presented in Figure 5, from which it can be seen that the RWA approximation is indeed valid for times for which "interaction frequency" $E_{int}/\hbar$ is smaller than the HO frequency ω. In a simulation involving the voltage flip at time t_1, fidelity decreases a bit after the flip but is still relatively high and satisfactory.

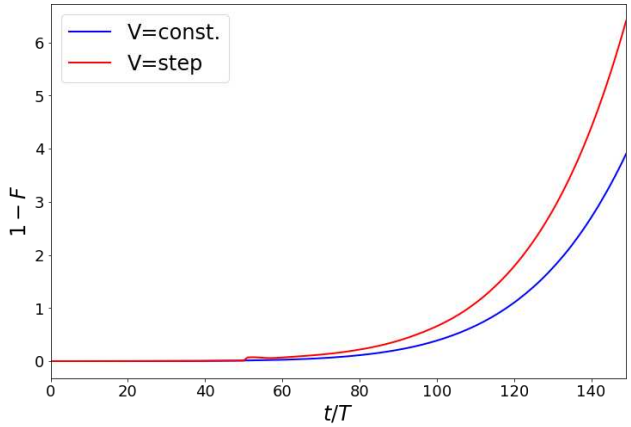

Figure 5. Validity of the RWA approximation: Blue curve represents infidelity $1 - F(t)$ Equation (18) for the time-protocol with constant bias voltage. The red curve represents infidelity for the time-protocol Equation (3) involving the step-function switching of the bias voltage and its polarity flip at the time instant $t_1 = 50.1\,T$. Calculations were carried out for the realistic parameters for which the RWA time is $t_{RWA} \approx 36\,T$ (time t is scaled to the period of mechanical vibration T).

4.3. The Off-Resonance Effects

In reality, it is hard to expect that it is experimentally possible to achieve exactly perfect resonance between mechanical frequency and Josephson's frequency, i.e., $\omega = l\Omega_J$. Although the bias voltage can be tuned with a precision of 0.1% [40], it produces a certain shift in the SC phase, leading to detuning from the resonant condition. The effect of the high-frequency noise, with frequency much higher than the operating frequency, is, on the

other hand, less pronounced since the corresponding phase shift averages itself to zero. We model the off-resonance effect by assuming that l is not a positive integer but rather a positive real number, close to the integer value. In the semiclassical approach, it can be shown that the qubit subsystem acts as a sinusoidal driving with frequency Ω_J for a mechanical harmonic oscillator of the frequency ω [45]:

$$\ddot{x} + \omega^2 x = f_0 \cos(\Omega_J t), \tag{19}$$

where $f_0 = 2\Omega_J|\epsilon C|$ and C is a constant that depends on system parameters. In the resonant case, $\omega = \Omega_J$, the solution of this equation of motion are oscillations with frequency Ω_J and amplitude linearly increasing in time, i.e.,

$$x(t) = \frac{f_0}{2\Omega_J} t \sin(\Omega_J t). \tag{20}$$

In the off-resonant case $\omega = l\Omega_J$, taking $l \approx 1$, solution of the equation of motion (19) are beats,

$$x(t) = \frac{2f_0}{\Omega_J^2(l^2-1)} \sin\left(\frac{\Omega_J}{2}(l-1)t\right) \sin\left(\frac{\Omega_J}{2}(l+1)t\right). \tag{21}$$

This solution has approximately linear-in-time growing amplitude as long as the argument of the first sinus function in Equation (21) is small, $\Omega_J(l-1)t/2 \ll 1$, i.e., when the sinus function can be expanded up to the linear term in a Taylor series. This condition determines the time interval along which building of standard coherent states, with amplitude that is linear in time, is preserved, depending on the parameter Ω_J and off-resonance parameter $l-1$.

In Figure 6a, the mean numbers of phonons before the voltage polarity flip, for several off-resonant cases, are shown. We see that numerically obtained phonon numbers follow amplitudes of the semi-classical solutions (21). The solution obtained in the off-resonant case represents a qubit entangled with a mechanical coherent state as in Equation (12), except that the amplitude is not increasing linearly in time, but rather oscillates slowly, beating with frequency $\Omega_J|l-1|/2$.

We wish to obtain the superposition of mesoscopically distinguishable states (coherent states that are nearly orthogonal), and that is why the obtained coherent states should be well separated in the phase space. As already mentioned, the distance of the coherent states is equal to twice the magnitude of their amplitude. However, in the non-resonant case, as explained above, the distance in the phase space does not increase linearly in time but rather performs slowly oscillating beats with the amplitude $2f_0/(\Omega_J^2(l^2-1))$. Thus, for the larger deviations from the resonant case, after the voltage flip, the nanomechanical cat-states will not be formed by the two (nearly) orthogonal coherent states but rather by the ones with large overlap. Even for small deviations from the resonance, the same problem will occur if the voltage flip occurs at the instant at which the coherent state amplitude is near the minimum of the amplitude oscillation function. If one wants coherent states to form the cat-states with an overlap smaller than the value ϵ_1, then, in the case of voltage flipping time t_1 coinciding with the maximum of the amplitude of the beat, the deviations from the resonance should be smaller than the threshold value given by

$$|l^2-1| < \frac{4f_0}{\Omega_J^2\sqrt{\ln(1/\epsilon_1)}}. \tag{22}$$

For example, with the realistic parameters used in numerical simulations, if one wants the overlap to be smaller than $\epsilon_1 = 10^{-8}$, deviations should not be larger than $|l^2 - 1| \approx 3\%$.

In Figure 6b,c, we show Wigner functions (17) for times $t > t_1$ for different deviations from the resonance. From these plots, we see that estimation for the resonance deviation threshold given above gives a good prediction when the superposition of orthogonal coherent states can be created. Since the bias voltage in the microvolt range can be controlled to a precision of ≈0.1% in the experiment, the corresponding Josephson frequency can be adjusted to be precise enough so that the resonance condition is fulfilled to the needed precision discussed in this section The (d) panel shows the Wigner function in the case when the offset from the resonance is larger than 3%, resulting in a wave function that does not correspond to the well-resolved cat-state.

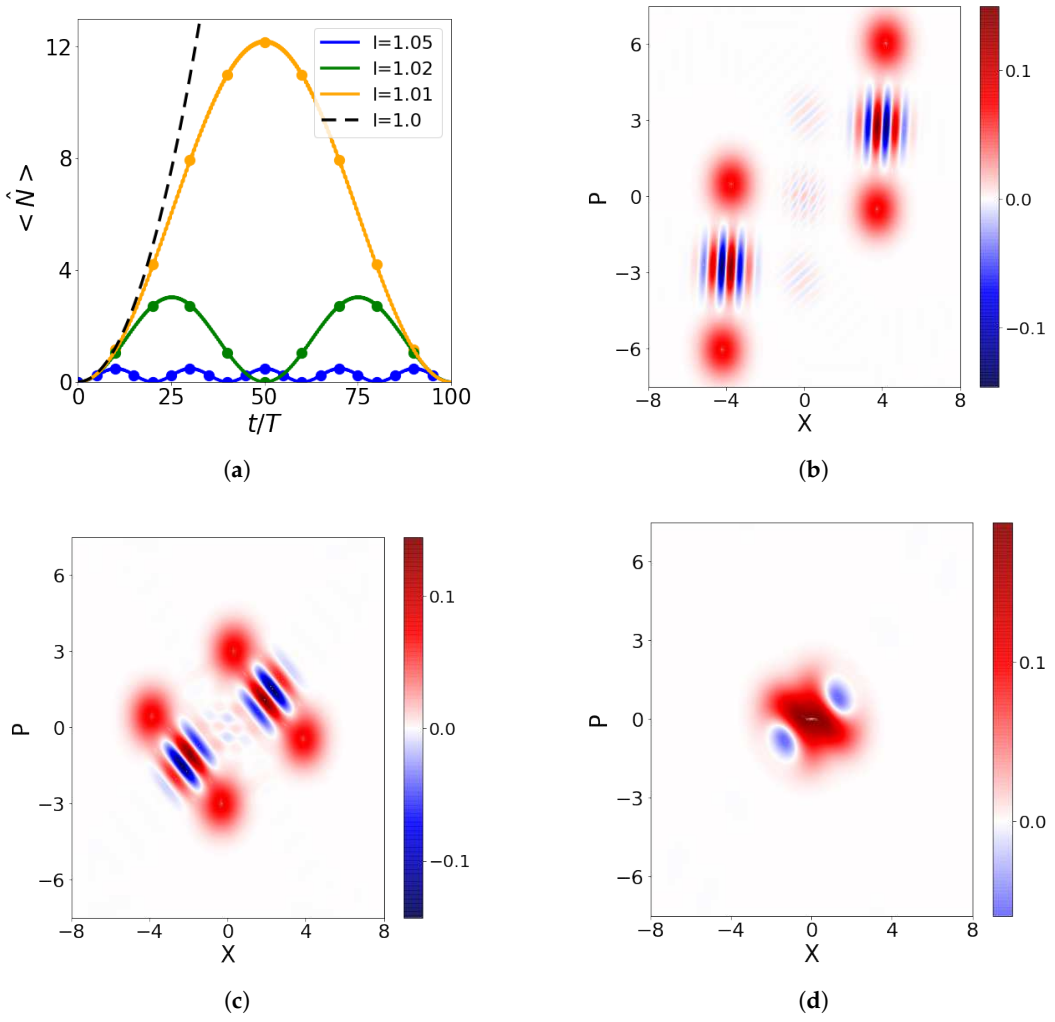

Figure 6. The off-resonance effects: (**a**) Mean number of phonons as a function of time for different deviations from the resonance condition, parametrised by l different from 1. Solid curves represent numerical solutions; dots represent analytical semi-classical solution (21). The dashed line represents the resonant case. (**b**–**d**) The Wigner function (17) for different deviations from resonance condition for times $t > t_1$, where t_1 is chosen so that the oscillations of the phonon number is near its maximum at the time of the voltage flip (time t is scaled to period T). In particular: (**b**) $l = 1.01$, $t_1 \approx 20.3\,T$; (**c**) $l = 1.02$, $t_1 \approx 25.7\,T$; (**d**) $l = 1.05$, $t_1 \approx 10.7\,T$. One can track the deterioration of the well-resolved cat-states as the offset from the resonance increases, namely (**b**,**c**) for less than 3% offset, and (**d**) for larger than 3%—see Equation (22) and comment below.

4.4. Deviation from the Voltage Flip Condition

Here we model how deviation from the ideal voltage polarity flip timing, determined by Equation (11), which can appear in a realistic experimental situation, affects the formation of the cat-states. As explained in Section 3, the cat-states are formed if the mean value of functions $g_3(t)$ and $g_4(t)$ are zero for $t > t_1$. However, conditions exist, namely timing of the voltage polarity flip t_1, for which the mean value of functions $g_1(t)$ and $g_2(t)$ is zero for $t > t_1$ rather than those of $g_3(t)$ and $g_4(t)$. As seen from Figure 7a, in that case, no cat-states are formed. This is because, for this kind of Hamiltonian, evolution for $t > t_1$ does not lead to splitting of the coherent states into cat-states, but rather to the change of the phase of the coherent state. In simulations of this effect, we choose a random voltage flip instant from the time interval $t_{flip} \in [t_1 - 0.1T, t_1 + 0.1T]$, where t_1 satisfies Equation (11). Figure 7b–d show three simulations with this kind of random t_{flip} time instants. We can see that, in this case, the cat-states are formed, but they are no longer symmetric. We ran a number of simulations with this kind of random voltage polarity flipping moment, and it turns out that most of them produced qualitatively the same result.

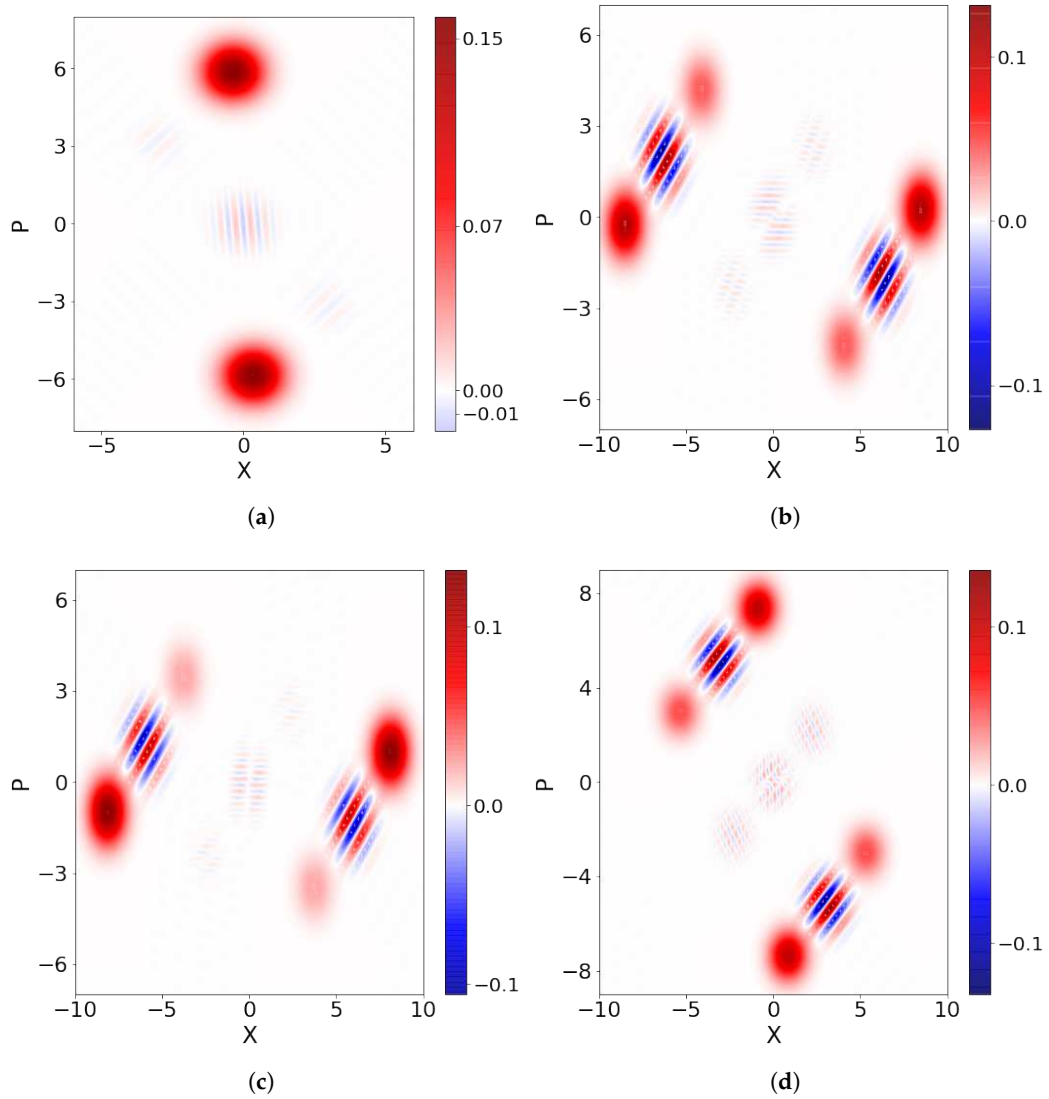

Figure 7. The Wigner functions for deviations from the condition Equation (11): (**a**) t_{flip} chosen "wrong" so that, even after the voltage polarity flip, the mechanical subsystem is simply a mixture of coherent states not forming a cat-state; (**b–d**) t_{flip} chosen randomly from the interval $t_{flip} \in [t_1 - 0.1T, t_1 + 0.1T]$, for which the non-symmetric cat-states are formed (T is period of mechanical oscillations).

4.5. Realistic Modelling of the Voltage Flip

So far, we considered a time protocol in which, at a specific time instant t_1, the voltage polarity is flipped instantaneously. This is experimentally unrealistic because some finite switching time T_{sw} is required to flip the voltage from the value V_0 to the value $-V_0$. We model such a protocol using the hyperbolic tangent function for the bias voltage profile, i.e.,

$$V(t) = -V_0 \tanh\left(\frac{t - t_1}{T_{sw}}\right), \tag{23}$$

where T_{sw} has now the role of characteristic time-scale of voltage polarity switching (see Figure 8a). In Figure 8b, the infidelity between the numerical solution with this protocol and the RWA solution with the step-function protocol is shown. As expected, as the switching time T_{sw} increases, the fidelity decreases. In the limit $T_{sw} \to 0$, we obtain the step-function protocol. In Figure 8c,d, the Wigner function of the mechanical subsystem for different values of T_{sw} is shown at times $t > t_1 + T_{sw}$. It can be seen that the formed cat-states are not symmetric, as in the case of the perfect step-function protocol, with asymmetry increasing as T_{sw} increases. The cat-states are also distorted to some extent.

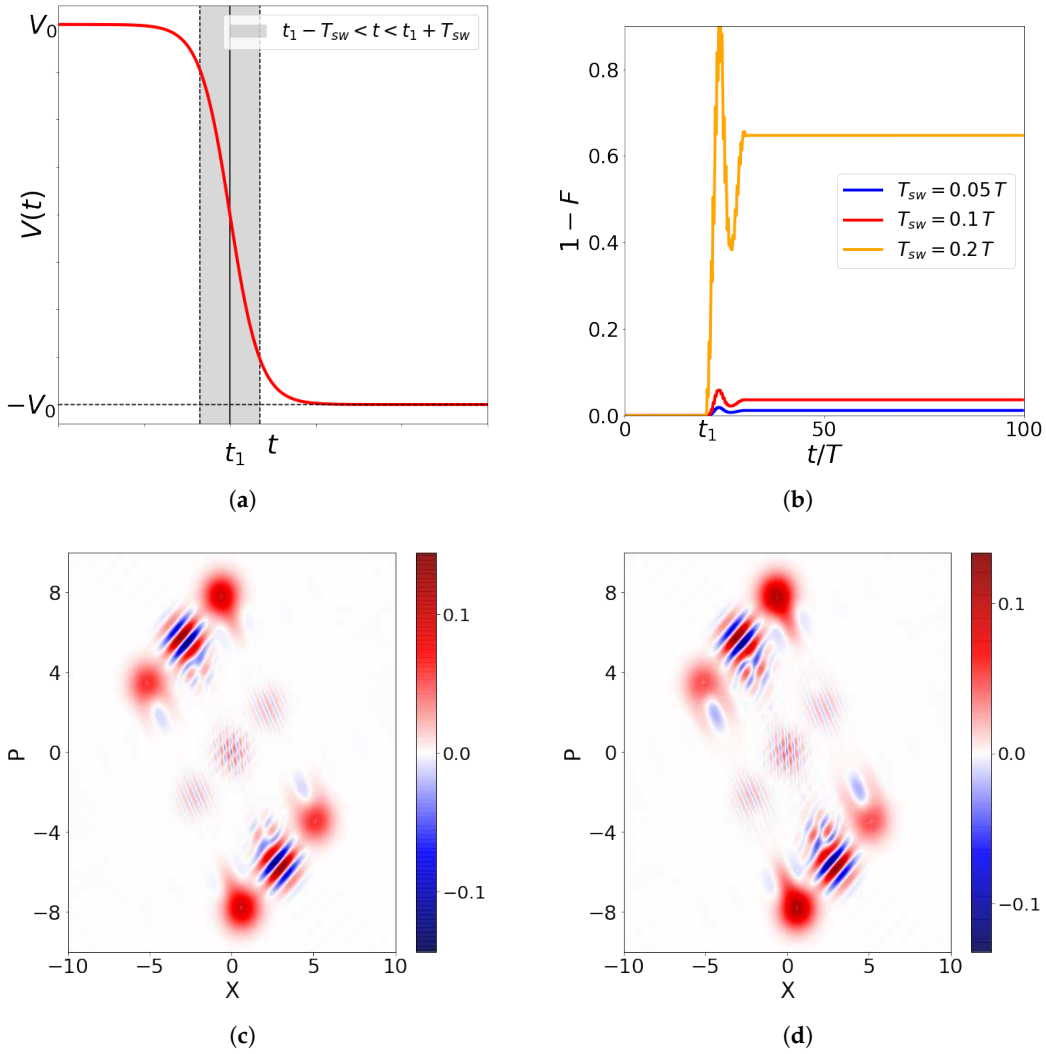

Figure 8. Realistic protocol for the bias-voltage flip: (**a**) the bias voltage $V(t)$ polarity flip time-protocol, Equation (23); (**b**) infidelity between the perfect step-function time protocol and the one with the voltage profile (23); (**c**,**d**) the Wigner functions for two different values of the voltage flip duration T_{sw}, i.e., $T_{sw} = 0.05\,T$ and $T_{sw} = 0.1\,T$, respectively (T is period of mechanical oscillations).

4.6. Decoherence Effects

In this section, we consider the coupling of the system to the environment, assuming that the mechanical and qubit subsystems couple to the environment independently. We analyse the effect of this coupling on the formation of the cat-states in terms of the phenomenological Lindblad master equation in the interaction picture

$$\frac{\mathrm{d}\hat{\rho}}{\mathrm{d}t} = -\frac{i}{\hbar}[\hat{H}_I, \hat{\rho}] + \Gamma_{loss}\left(\hat{a}(t)\hat{\rho}\hat{a}^\dagger(t) - \frac{1}{2}\{\hat{a}^\dagger(t)\hat{a}(t), \hat{\rho}\}\right) + \Gamma_{flip}\left(\hat{\sigma}_x\hat{\rho}\hat{\sigma}_x - \frac{1}{2}\{\hat{\sigma}_x\hat{\sigma}_x, \hat{\rho}\}\right), \quad (24)$$

where $\hat{a}(t) = e^{-i\omega t}\,\hat{a}$. We assume that the most dominant decoherence process for the mechanical subsystem is through the phonon loss process, while the most dominant decoherence process for the qubit subsystem is through the flip of the charge qubit states. In the master equation, the phonon loss is described by the phonon annihilation operator $\hat{a}$ and characterized by the "phonon loss rate" Γ_{loss}, while the qubit state flip is described by the Pauli $\hat{\sigma}_x$ operator and characterized by the "charge qubit flipping rate" Γ_{flip}. Phonon loss rate Γ_{loss} can be determined from the quality factor $Q = \omega/\Delta\omega \approx \omega/\Gamma_{loss}$. For mechanical frequency in the GHz range, which we used in simulations, a rather conservative value for the Q factor that we used is $Q = 1000$ (quality factors of nanomechanical resonators in this frequency range can be an order of magnitude higher or more [15–17]). This yields a characteristic phonon loss time scale of $\Gamma_{loss}^{-1} \approx 44\,\mathrm{ns} \approx 160\,T$. For the charge qubit decoherence (charge flipping) time scale, we took $\Gamma_{flip}^{-1} \approx 0.04\,\mu\mathrm{s} \approx 150\,T$, even though current state-of-the-art experiments work with charge qubits with decoherence times as large as $\Gamma_{flip}^{-1} \approx 1\,\mu\mathrm{s}$.

4.6.1. Effect of the Phonon Loss

In this subsection, we model the effect of phonon loss alone in the absence of qubit state flipping (i.e., $\Gamma_{flip} = 0$). One of the obvious effects of the phonon loss process is the reduction of the amplitude of the coherent state. To examine this, in Figure 9a, we plot the mean number of phonons for a system evolution with $\Gamma_{loss} = 0$ and for several values of $\Gamma_{loss} \neq 0$. As expected, the amplitude of a coherent state decreases as the phonon loss rate increases. Due to the partially non-coherent evolution caused by the interaction of the system with the environment, the state of the system is no longer a pure state but rather a mixed one. To quantify this, we calculate a time evolution of the purity of the total state of the system

$$\gamma(t) = \mathrm{Tr}\left(\hat{\rho}(t)^2\right). \quad (25)$$

For a pure state, $\gamma = 1$, tending to decrease as the state becomes more mixed, which happens over time as the decoherence effect becomes more important (see Figure 9b). To model this mixed state, we analyse how many and which states contribute to the state of the system. It is done by decomposing the density matrix by diagonalising it, i.e.,

$$\hat{\rho}(t) = \sum_k p_k(t)|\psi_k(t)\rangle\langle\psi_k(t)|, \quad (26)$$

where $|\psi_k(t)\rangle$ is the eigenstate with kth largest eigenvalue. Eigenvalue $p_k(t)$ represents the probability of finding a system in the state $|\psi_k(t)\rangle$. For a pure state, there is only one $p_1 = 1$, i.e., for all the other states, $p_k = 0$, $k > 1$, while for a mixed state, more than one state has $p_k \neq 0$. Interestingly, for our system with only the phonon loss decoherence process included, there is a finite number of states with $p_k \neq 0$. Namely, before the voltage flip, the density matrix is a mixture of two states, $|\psi_1\rangle$ and $|\psi_2\rangle$, and, after the flip, it becomes a

mixture of four states (see Figure 9d). To explain one extra state before the voltage polarity flip, we first notice that $\hat{\tilde{H}}_I(t)$ from Equation (9) commutes with the parity operator

$$\hat{P}_{Nx} = (-1)^{\hat{N}}\sigma_x \tag{27}$$

thus preserving the parity symmetry [31]. This operator has only two eigenvalues, $P_{Nx} = \pm 1$. Since the initial state of the system has its well-defined value $P_{Nx} = +1$, the state of the system Equation (12), after the coherent evolution, also has $P_{Nx} = +1$. On the other hand, operator $\hat{a}$ does not preserve parity since $[\hat{a}, \hat{P}_{Nx}] \neq 0$. Therefore, by introducing the non-coherent phonon loss process described by it, the state with negative parity will also be accessed by the evolution of the system. From this reasoning and numerical analysis, we conclude that, for times $t < t_1$, we have

$$\begin{aligned} |\psi_1(t < t_1)\rangle &\approx \frac{1}{\sqrt{2}}\Big(|+\rangle \otimes |\alpha_1(t)\rangle + |-\rangle \otimes |-\alpha_1(t)\rangle\Big), \\ |\psi_2(t < t_1)\rangle &\approx \frac{1}{\sqrt{2}}\Big(|+\rangle \otimes |\alpha_1(t)\rangle - |-\rangle \otimes |-\alpha_1(t)\rangle\Big). \end{aligned} \tag{28}$$

Here, $|\psi_1(t)\rangle$ is basically the state from Equation (12) obtained from the RWA solution, a bit distorted (it has lower amplitude due to phonon loss from the coherent state and their moving to nearby states), while the state $|\psi_2(t)\rangle$ is the state corresponding to it, but with negative parity. To summarize, for times $t < t_1$, the phonon loss process does two things: (i) produces a mixed state by introducing an extra state that is the same as the one obtained from the coherent evolution but with negative parity, and (ii) reduces the amplitude of the coherent states (phonon number) by shifting the occupation in the Hilbert space from "coherent" to the "non-coherent part".

After the voltage polarity flip, two extra states appear in the system's evolution. All of them have a well-defined parity (two states have positive, and the other two have negative parity). This extra splitting can be explained. Just before the voltage flip, the state of the system is a mixture of a state with positive parity $|\psi_1(t_1)\rangle$ and a state with negative parity $|\psi_2(t_1)\rangle$. After the voltage flip, those states change differently: $|\psi_1(t)\rangle$ is changed to $|\tilde{\psi}_1(t)\rangle$, which is equal to the solution for coherent evolution of the entangled cat-state with positive parity (see Equation (12)), while the state $|\psi_2(t_1)\rangle$ is changed to $|\tilde{\psi}_2(t)\rangle$, a state with the negative parity (because the Hamiltonian preserves parity). However, $|\tilde{\psi}_2(t)\rangle$ is no longer the same state as $\tilde{\psi}_1(t)$ with the opposite parity. Namely, the cat-states forming it are no longer given by Equations (14) and (15), but rather by

$$|\tilde{\psi}_+\rangle = \Big(\beta|-\alpha_1-\alpha_2\rangle + i\beta^*|\alpha_1-\alpha_2\rangle\Big), \tag{29}$$

$$|\tilde{\psi}_-\rangle = \Big(\beta^*|-\alpha_1+\alpha_2\rangle + i\beta|\alpha_1+\alpha_2\rangle\Big). \tag{30}$$

Since the phonon loss operator does not preserve parity, a state $|\tilde{\psi}_3(t)\rangle$, with the negative parity, will appear in the system dynamics due to incoherent mixing of the positive parity state $|\tilde{\psi}_1(t)\rangle$. Similarly, a state $|\tilde{\psi}_4(t)\rangle$, with positive parity, will appear in the system dynamics from the negative parity state $|\tilde{\psi}_2(t)\rangle$.

It is also worth noticing that, after a sufficiently long time, a state with a positive parity, which resembles the coherent evolution state from Equation (12), is no longer the most dominant state in the mixture. To illustrate that the discussed eigenstates of the density matrix are indeed cat-states, we plot the Wigner functions of the reduced density matrix of the mechanical subsystem of all of the non-vanishing states $|\psi_k\rangle$, $k = 1, 2, 3, 4$ (see Figure 10).

Since the state of the system in the presence of phonon loss is no longer pure, we can not use the entropy of entanglement properly to quantify entanglement between the qubit and the mechanical subsystem. That is why we use so-called negativity as a measure of the entanglement, which is more suitable for mixed states, i.e.,

$$\mathcal{N}(\hat{\rho}) = \frac{||\hat{\rho}^{T_q}||_1 - 1}{2}, \tag{31}$$

where $||X||_1 \equiv \mathrm{Tr}\sqrt{X^\dagger X}$ and $\hat{\rho}^{T_q}$ is a partial transpose with respect to qubit DOFs [46]. In Figure 9c, we present the influence of phonon loss on entanglement negativity. As we can see, entanglement is generally smaller for larger phonon loss rates. Negativity reaches its maximum (0.5 for a pure state) and then decreases with time, as the decoherence effects become more pronounced, and reaches 0 for times large enough. However, the purity and negativity decrease rate do not only depend on the phonon loss rate Γ_{loss} but also on the coupling parameter ϵ through the mean phonon number (see Appendix A for clarification).

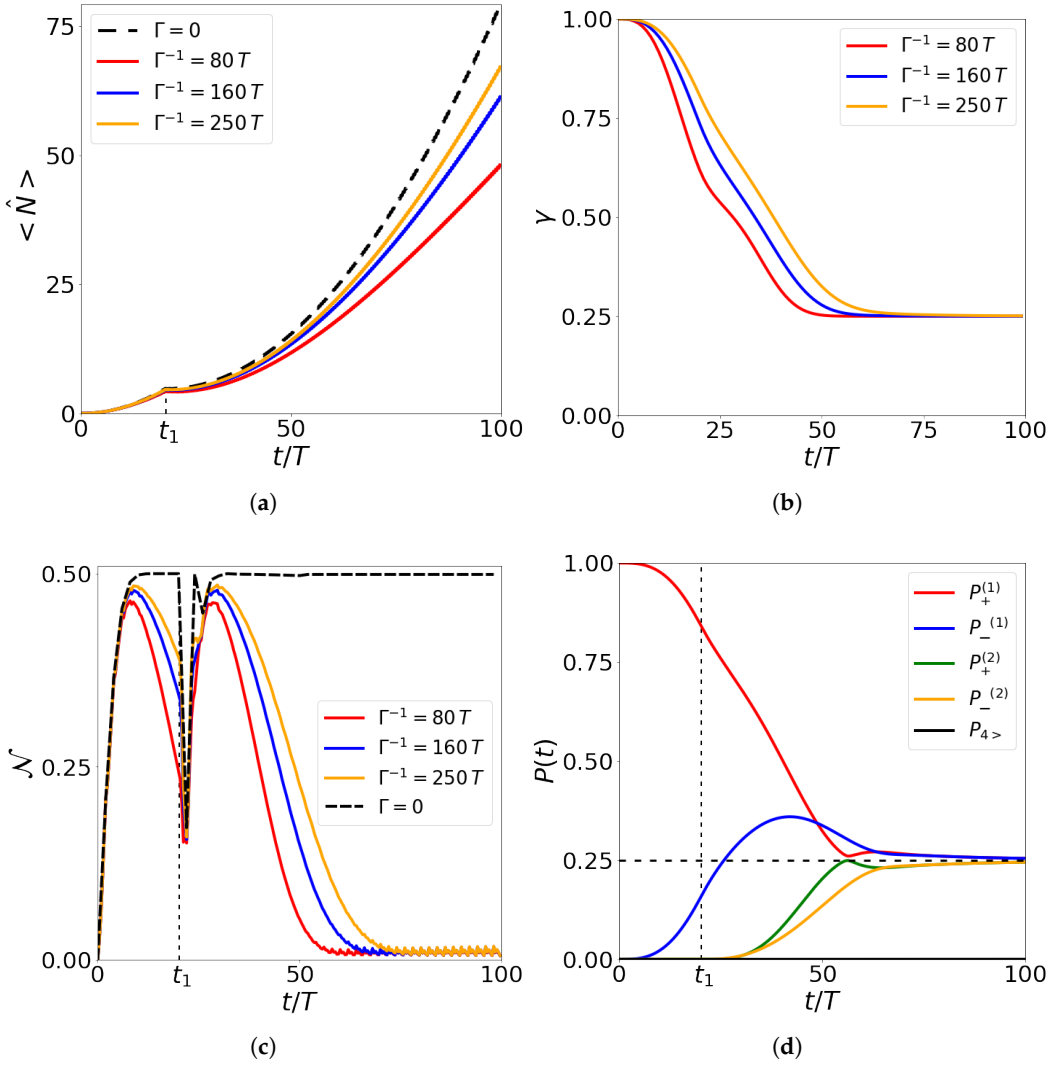

Figure 9. Effects of the phonon loss (with characteristic rate $\Gamma \equiv \Gamma_{loss}$, see Equation (24) and explanation below): (**a**) the mean number of phonons in time—dashed line represents coherent evolution without phonon loss process, full lines are for different phonon loss rates; (**b**) purity of a state, Equation (25)—at $t = 0$ the state is pure, i.e., $\gamma = 1.0$, getting saturated at $\gamma = 0.25$ in the steady state; (**c**) entanglement negativity, Equation (31)—dashed curve represents negativity for the purely

coherent evolution, for which it reaches the maximum value of 0.5 (entanglement of a Bell state). For the non-coherent evolution, negativity first increases and then saturates to 0 (the non-entangled state) in the steady state; (**d**) the density matrix eigenvalues from Equation (26) for $\Gamma_{loss}^{-1} = 160\,T$—red and green curve represent probability of finding states with the positive parity, while blue and orange ones represent probability of finding states with the negative parity (time t is scaled to period of mechanical oscillations T).

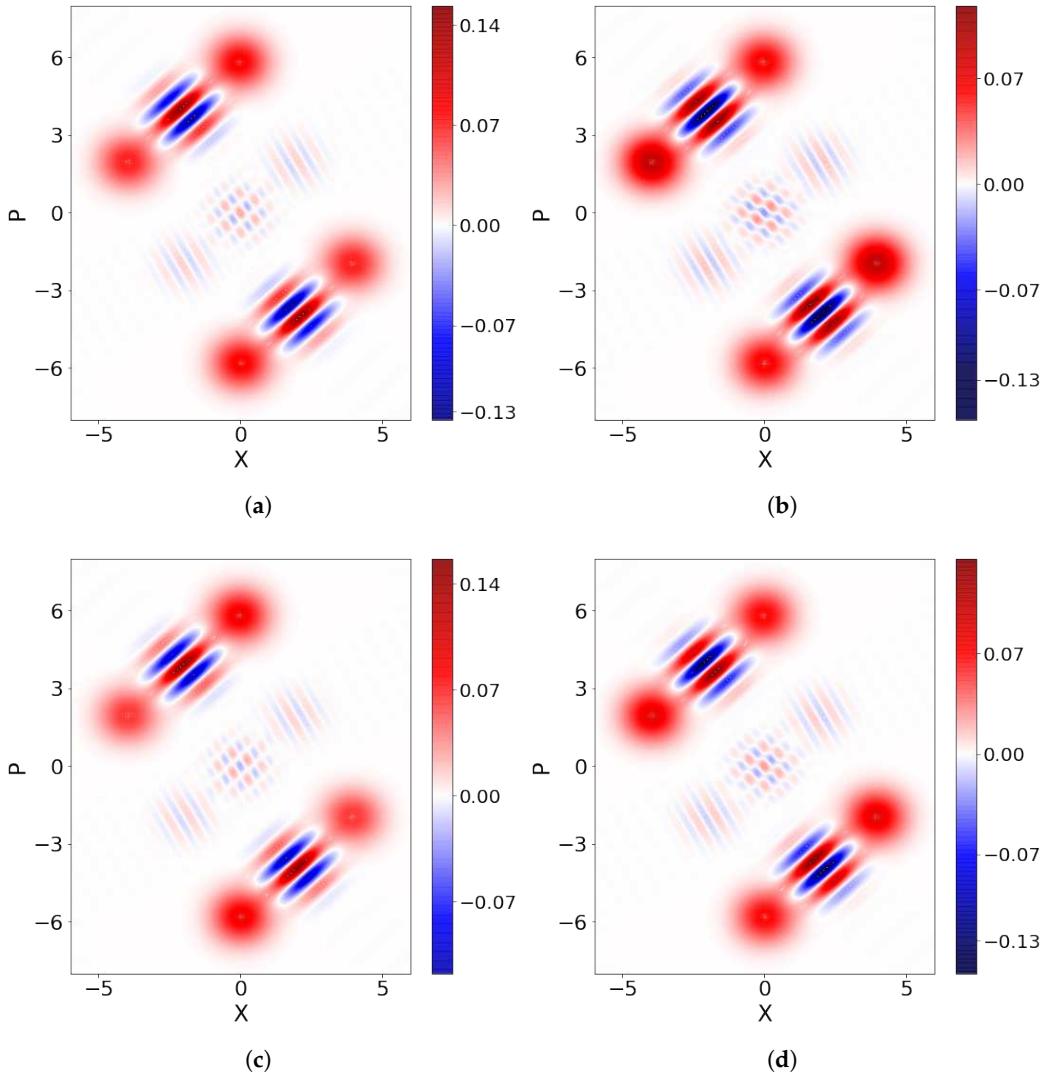

Figure 10. Wigner function of four non-vanishing eigenstates of the density matrix (see Equation (26) and explanation below) under the evolution, with phonon loss process ($\Gamma_{loss}^{-1} = 160\,T$), for time $t = 50\,T$. It can be seen that states $|\tilde{\psi}_1(t)\rangle$ and $|\tilde{\psi}_3(t)\rangle$ are the same states up to parity (parity cannot be observed on the mechanical subsystem only), and equivalently for states $|\tilde{\psi}_2(t)\rangle$ and $|\tilde{\psi}_4(t)\rangle$. Panels show: (**a**) state $|\tilde{\psi}_1(t)\rangle$; (**b**) state $|\tilde{\psi}_2(t)\rangle$; (**c**) state $|\tilde{\psi}_3(t)\rangle$; (**d**) state $|\tilde{\psi}_4(t)\rangle$.

4.6.2. Effect of the Qubit State Flipping

In this subsection, we model the effect of the charge qubit state flip in the absence of phonon loss (i.e., $\Gamma_{loss} = 0$). By calculating the time-evolution of the purity of the state (Figure 11a), we see that, due to the non-coherent qubit flips, the state of the system is no longer pure but a mixture. By analysing the state (expanding density matrix as in Equation (26)), we conclude that, for sufficiently small times, only one state dominates, while others have low probabilities of being found (see Figure 11c,d). This is qualitatively different from the effect of phonon loss, since there we have two (four) non-zero probability states participating in the system evolution before (after) the voltage polarity flip. That is because, unlike the annihilation operator $\hat{a}$, the operator $\hat{\sigma}_x$ preserves the parity. Another

difference comparing to the phonon loss process is that, for the qubit flip effect, the non-vanishing states of the mixture (apart from the most important one) are no longer coherent (cat) states before (after) the voltage flip (see Figure 12).

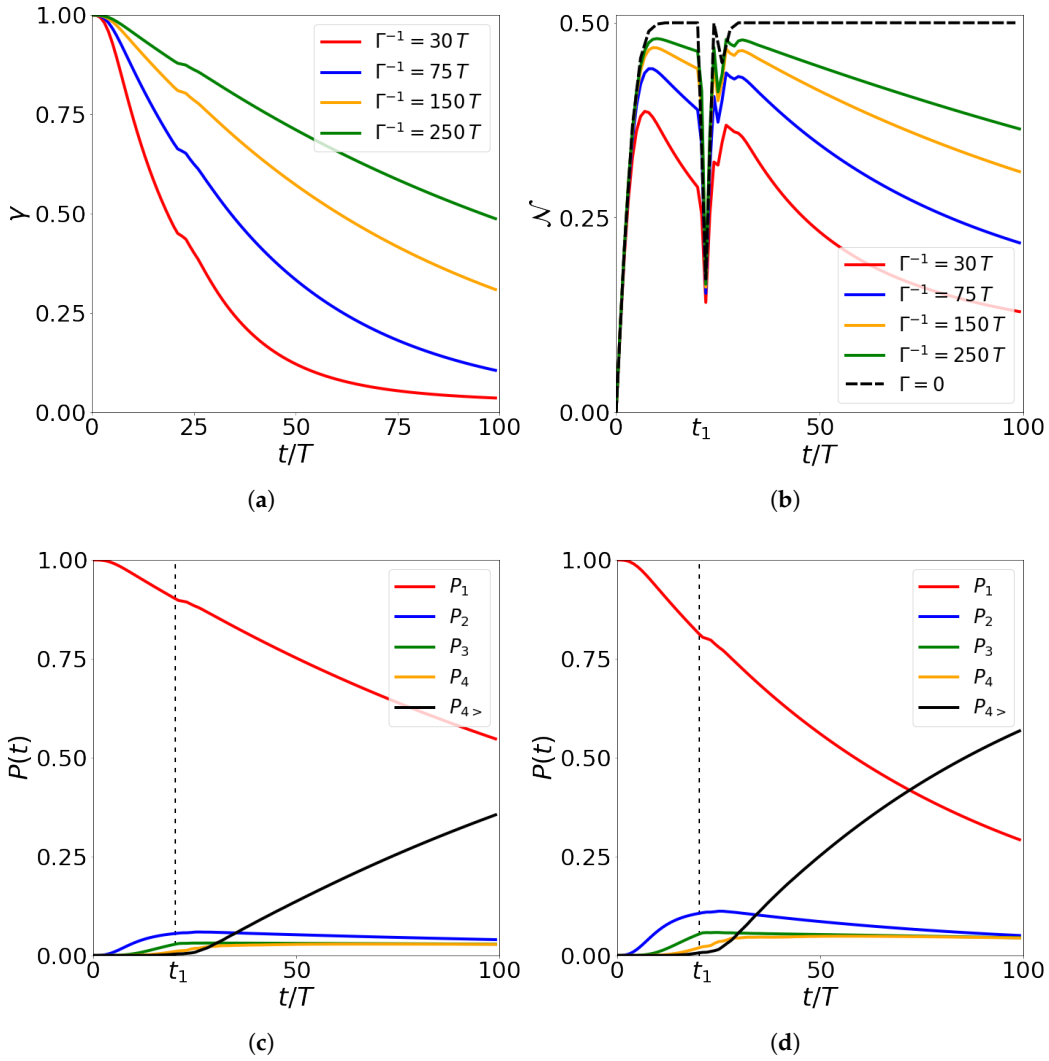

Figure 11. Qubit state flipping effect for different values of qubit flip rate (with characteristic rate $\Gamma \equiv \Gamma_{flip}$, see Equation (24) and explanation below): (**a**) purity of a state, Equation (25)—at $t = 0$ the state is pure, i.e., $\gamma = 1.0$, decreasing to the value close to zero at the time scales $t \gtrapprox \Gamma_{flip}^{-1}$; (**b**) entanglement negativity, Equation (31)—dashed curve represents negativity for the coherent evolution, for which it reaches the maximum value of 0.5 (entanglement of a Bell state). For the non-coherent evolution, negativity first increases and then decreases to 0 (non-entangled state); (**c**) eigenvalues of the density matrix from Equation (26) for $\Gamma_{flip}^{-1} = 150\,T$; (**d**) eigenvalues of the density matrix from Equation (26) for $\Gamma_{flip}^{-1} = 75\,T$ (T is period of mechanical oscillations).

Finally, we study entanglement between the qubit and mechanical subsystem, with the present qubit flip process, by calculating negativity. As can be seen from Figure 11b, the entanglement negativity increases at first, but for times $t \gtrapprox \Gamma_{flip}^{-1}$ it tends to decrease, saturating to zero.

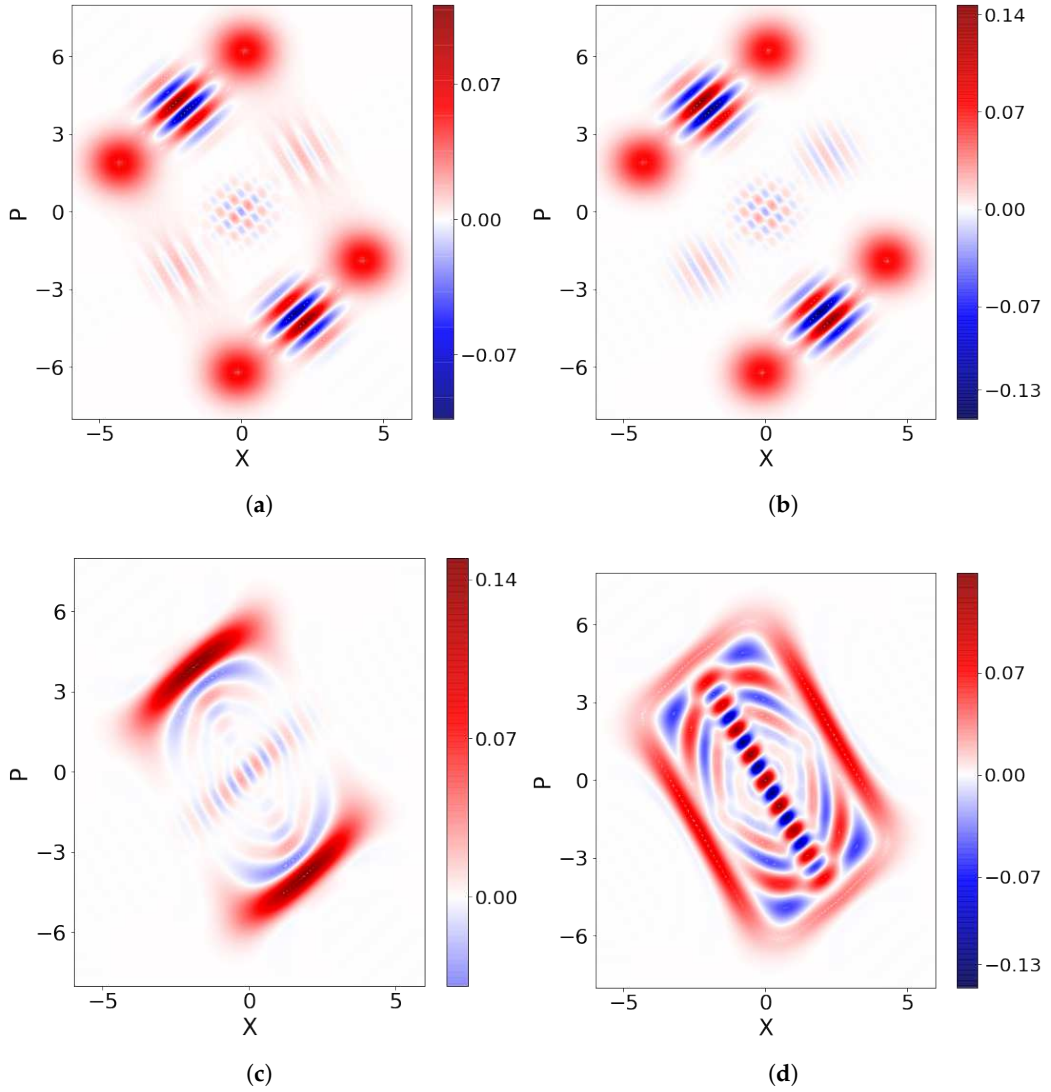

Figure 12. The Wigner function with the effect of qubit state flipping ($\Gamma_{flip}^{-1} = 150\,T$), for time $t = 50\,T$: (**a**) the Wigner function of the the total state, i.e., the density matrix $\rho\hat{(}t)$, Equation (26); (**b**–**d**) Wigner functions of the first three eigenstates of the density matrix with the highest eigenvalues, i.e., $|\tilde{\psi}_1(t)\rangle$, $|\tilde{\psi}_2(t)\rangle$, $|\tilde{\psi}_3(t)\rangle$, respectively. It can be seen that only the most probable state (**b**) is a cat-state, while the other states participating in the dynamics are not cat-states.

4.6.3. Effect of Combined Qubit State Flipping and Phonon Loss

In this subsection, we study time-evolution under the influence of both qubit flip and phonon loss processes. The most dominant state in a mixture is an entangled coherent (cat) state with positive parity before (after) the voltage polarity flip. Two (four) most dominant non-vanishing states participating in the mixture are coherent (cat-states), but now also other states (but with lower eigenvalues) participate in the system dynamics due to the qubit flip decoherence process (see Figure 13, in particular panel (d)). To check that the first four states after the voltage flip are indeed entangled cat-states, while the other less-significant states are not, we plotted the Wigner function in Figure 14.

The mean number of phonons is lower than in the case of coherent evolution due to the phonon loss process. Finally, as can be seen from Figure 13c, entanglement negativity decreases basically to zero for times $t \gtrapprox \Gamma_{flip}^{-1}$.

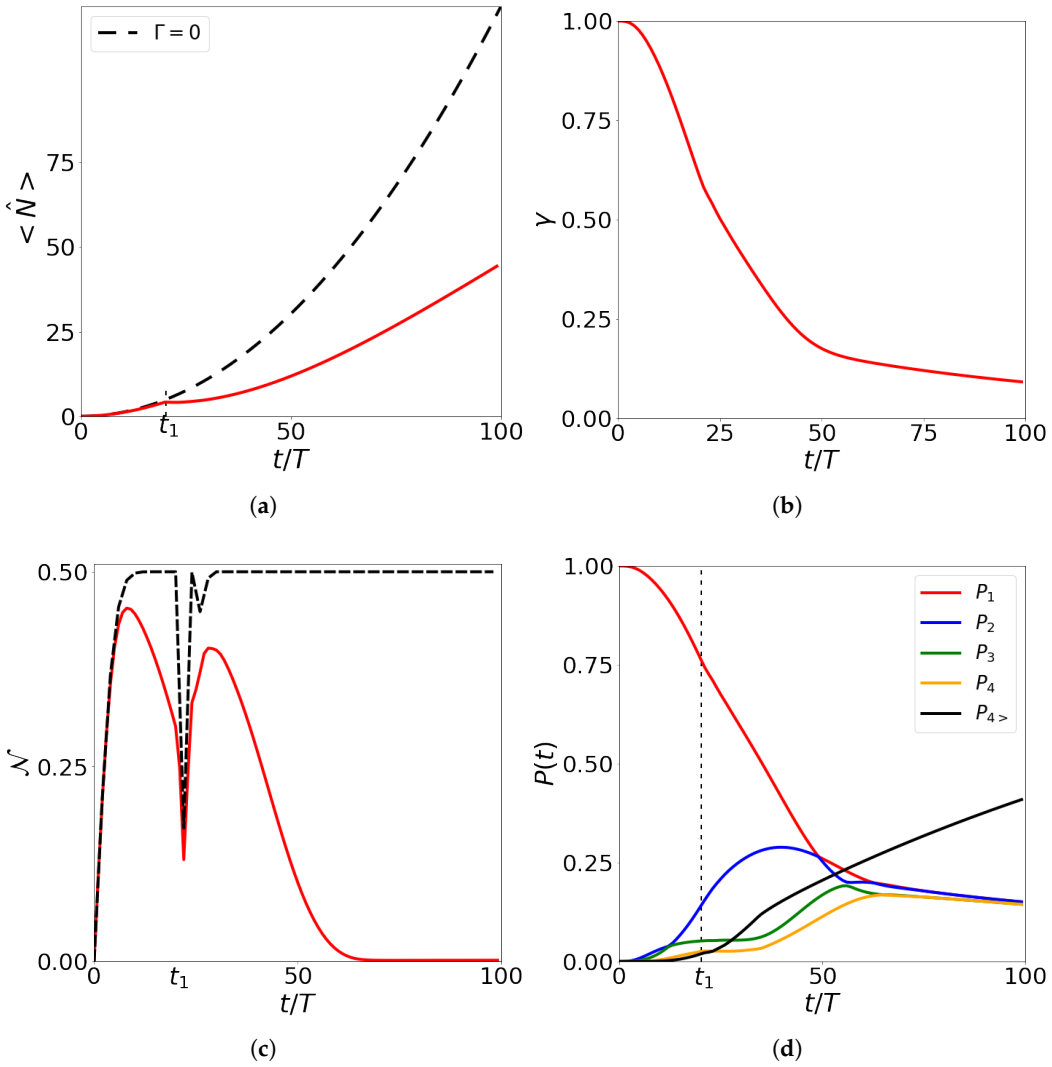

Figure 13. Effect of combined phonon loss and qubit flip process as a function of time for $\Gamma_{loss}^{-1} = 160\,T$, $\Gamma_{flip}^{-1} = 150\,T$ (black dashed line represents coherent evolution without decoherence): (**a**) mean number of phonons; (**b**) purity of a state, Equation (25); (**c**) entanglement negativity, Equation (31); (**d**) density matrix, Equation (26), eigenvalues. Red and green curves represent the probability of finding states with positive parity, while blue and orange ones represent the probability of finding states with negative parity. Not only do the entangled cat-states participate in the dynamics of the system, but other non-cat-states do as well (time is scaled to period of mechanical oscillations T).

One should note that the result simply presents both decoherence channels acting at the same time, not the interaction between the two. The subtle possibility of coupling of the decoherence sources arises due to coupling of the oscillator and qubit, i.e., $\epsilon \neq 0$. If coupled, i.e., hybridised, the fluctuation of phonon number may change the qubit state and vice versa. However, compared to the "single decoherence source" effect, appearing with ϵ^0, the "joint decoherence source" effect appears with ϵ^2, in the lowest order. As all our analysis is constructed and performed under the assumption of the weak coupling, $\epsilon \ll 1$, these effects are neglected in our consideration.

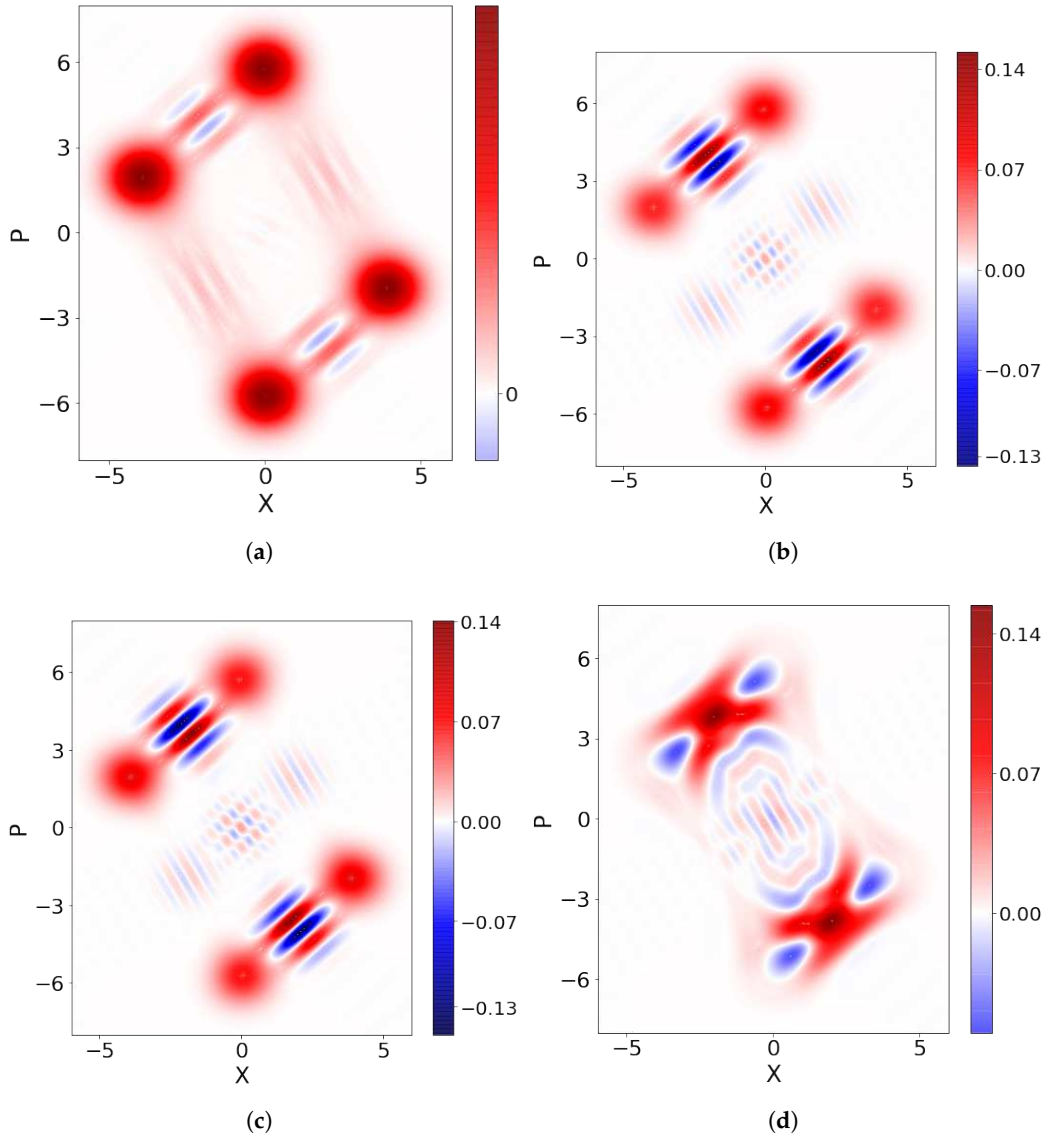

Figure 14. The Wigner function with the effect of qubit state flip ($\Gamma_{flip}^{-1} = 150\,T$) and the phonon loss ($\Gamma_{loss}^{-1} = 160\,T$), for $t = 50\,T$. The Wigner function of: (**a**) the the total state, i.e., the density matrix $\hat{\rho}(t)$, Equation (26); (**b**) the most dominant state $|\tilde{\psi}_1(t)\rangle$; (**c**) the fourth most dominant state $|\tilde{\psi}_4(t)\rangle$; (**d**) the fifth most dominant state $|\tilde{\psi}_5(t)\rangle$.

5. Conclusions

In conclusion, we study a nanoelectromechanical system, based on the AC Josephson effect, in which a superconducting mesoscopic grain in the regime of the Cooper pair box (CPB) performs harmonic oscillations between two bulk superconductors. By doing so, it couples its electric (charge qubit) and mechanical degrees of freedom, which depend on the position of the grain. The bias voltage controls a relative phase between bulk superconductors and, in turn, the evolution of the CPB states. Applying the time-protocol of manipulation with the bias voltage upon the system, the nanomechanical cat-states (quantum superposition of two mechanical coherent states) entangled with qubit states are generated, which, according to the analytical solution within the RWA approximation, crucially depend on resonant dynamics between the charge qubit and the mechanical oscillator. Throughout extensive numerical simulations, we check the validity of the approximate analytical solution and simulate a number of effects appearing in realistic experiments, which deteriorate resonant dynamics, to estimate the margin of experimental feasibility of cat-states formation. Namely, we study experimental limitations regarding the

precision of bias voltage time-protocol as well as decoherence processes related to phonon loss and qubit state flipping during the system evolution leading to coherent states and, in turn, to cat-states formation.

For a set of realistic experimental parameters, we find that the formation of cat-states is within experimental reach. In particular, for the order of magnitude of Josephson energy $10 \div 100\,\mu\text{eV}$, mechanical frequency 10 GHz (e.g., the third bending mode of the 1 μm single-wall suspended carbon nanotube), bias voltage 10 μeV (controllable down to 0.1%), mass of the mesoscopic grain $10^{-22} \div 10^{-21}$ kg (aluminium slab 20 nm long with radius 3 nm), amplitude of the harmonic oscillator zero-mode oscillations 1 pm, Cooper pair tunnelling lengths 0.1 nm, small coupling parameter $0.01 \div 0.1$, charge qubit 1 μs, and quality factor of mechanical oscillator 10^4, we find that formation of the cat-states should be experimentally feasible within the order of 10^2 periods of mechanical oscillations. This should yield well-separated (orthogonal) cat-states.

Well-formed cat-sates have the potential to be used in a number of applications. One possible direction is a "buffer" in the process of transduction of quantum information, using suitable protocols, among which one was suggested in Ref. [32], with the aim of transporting it among qubits, such as suggested in Ref. [47]. Very briefly described, such a transduction process is achieved by carefully tailored time-protocols for operating the external parameters, the bias voltage, and the gate voltage. One starts with the prepared state of charge qubit, with the quantum information encoded into the relative phase of two qubit states, and the oscillator in the ground state. Using the bias-voltage protocol, one builds the entangled charge qubit state with the well-developed mechanical coherent states (as described in this paper). Disconnecting the bias and operating the precisely set gate voltage, one can then perform a "unitary rotation in the opposite direction" upon the charge qubit states, being entangled with the "opposite" coherent states, to bring them to the same state. After that step, one ends with the pure nanomechanical cat-state with the quantum information encoded into the mechanical phase. Coupling several qubits and using the time-protocols upon the operating parameters permits the use of the entanglement as a powerful tool in transduction and transfer of quantum information, as suggested in the aforementioned references. Compared to the alternative mechanisms for generating mechanical cat-states, such as optomechanical, or the Kerr nonlinearity systems, for example, potentially the most rewarding difference is the aspect of sensitivity of control and size of the device. As the the optical-based alternatives rely on the radiation pressure for coupling of light to mechanics, or building a strong enough nonlinearity, which are both weak, in the system proposed here, in spite of the weak coupling to the superconducting Josephson circuit that coherently "pump" the cat-states, the better sensitivity in the sense of manipulation of the cat-states is achieved through the control of the charge qubit states by the gate voltage (see, e.g., Ref. [32]). Systems that rely on optical cavity are also considerably larger in size, i.e., of the order of centimetres for Fabry–Pérot, or millimetres for the microwave–superconductor implementation, down to 10^1–10^2 μm for photonic crystal cavities, still larger than the micrometre-size NEMS proposed here.

Author Contributions: M.T.—numerical modelling and calculations, analytical calculations, methodology, visualisation, writing—original draft preparation; D.R.—problem setup, conceptualisation, analytical modelling, visualisation, validation, writing—review and editing, project administration, and funding acquisition. All authors have read and agreed to the published version of the manuscript.

Funding: This work was supported by the Croatian Science Foundation, project IP-2016-06-2289 and by the QuantiXLie Centre of Excellence, a project cofinanced by the Croatian Government and European Union through the European Regional Development Fund—the Competitiveness and Cohesion Operational Programme (Grants KK.01.1.1.01.0004 and PK.1.1.02).

Data Availability Statement: The original contributions presented in this study are included in the article. Further inquiries can be directed to the corresponding author.

Conflicts of Interest: The authors declare no conflicts of interest whatsoever.

Appendix A. Eigenstate Probabilities

As noted in the main text, due to the symmetry of the Hamiltonian with respect to the parity operator (27), in the case of coherent evolution, only the state with positive parity (such as in Equation (12)) participates in the dynamics of the system. However, by introducing the phonon loss operator $\hat{a}(t)$, which does not preserve this symmetry, a state with negative parity is introduced in the system, and the total state of the system becomes a mixture of the two. Those two states, apart from the parity, are exactly the same, and the total Liouville operator from the master Equation (24) treats those two states in a symmetric way (because of the broken symmetry). Thus, in a steady state, the probability p_+ of finding the state with positive parity should be equal to the probability p_- of finding the state with negative parity:

$$p_+(t \to \infty) = p_-(t \to \infty) = \frac{1}{2}. \tag{A1}$$

From master Equation (24), we conclude that the rate at which the probability difference $\Delta p = p_+ - p_-$ of those two states changes is governed by the equation

$$\frac{\mathrm{d}\Delta p}{\mathrm{d}t} = -2\Gamma_{loss}\langle \hat{N}(t)\rangle \Delta p. \tag{A2}$$

Factor 2 appears by summing the equations for $\frac{\mathrm{d}p_1}{\mathrm{d}t}$ and $-\frac{\mathrm{d}p_2}{\mathrm{d}t}$; $\langle \hat{N}(t)\rangle$ is the average number of phonons that comes from the action of operators $\hat{a}$, $\hat{a}^\dagger$ on the state $\hat{\rho}$ of the right-hand side of Equation (24). The solution to the equation is easily obtained as

$$\Delta p(t) = \Delta p(t=0) \exp\left(-2\Gamma_{loss}\int_0^t \langle \hat{N}(s)\rangle ds\right). \tag{A3}$$

The expectation value can be found by using a semi-classical approach and solving the damped-driven harmonic oscillator equation

$$\ddot{x} + \Gamma_{loss}\dot{x} + \omega^2 x = f_0 \cos(\omega t). \tag{A4}$$

Solution to this equation with the initial condition $x(0) = \dot{x}(0) = 0$ is

$$\begin{aligned} x(t) &= \frac{f_0}{\omega\Gamma_{loss}\Omega}\left(-\omega e^{-\frac{\Gamma_{loss}t}{2}}\sin(\Omega t) + \Omega \sin(\omega t)\right), \\ \Omega &= \sqrt{\omega^2 - \left(\frac{\Gamma_{loss}}{2}\right)^2}. \end{aligned} \tag{A5}$$

Expectation value is now given by the square of the time-average of $x(t)$. Time-average is obtained by neglecting the oscillation terms, i.e.,

$$\langle \hat{N}(t)\rangle = \left(\frac{f_0}{\omega\Gamma_{loss}\Omega}\right)^2\left(-\omega e^{-\frac{\Gamma_{loss}t}{2}} + \Omega\right)^2. \tag{A6}$$

We plug in Equation (A6) into Equation (A3) and integrate the right-hand side to obtain the final solution; $P_+(t)$ and $P_-(t)$ are obtained by using $P_+(t) + P_-(t) = 1$. In Figure A1a, we compare these analytical results to the numerical ones. From this result, it can be concluded that the probability $p_2(t)$ and thus the purity $\gamma(t)$ and entanglement negativity do not

depend only on the rate Γ_{loss}, but on the phonon number as well. The state becomes more mixed as the phonon number increases; thus, for larger values of the coupling parameter ϵ, the state will become less pure faster. To see the influence of different values of ϵ and Γ on entanglement, in Figure A1b we plot negativity for different values of both ϵ and Γ_{loss}.

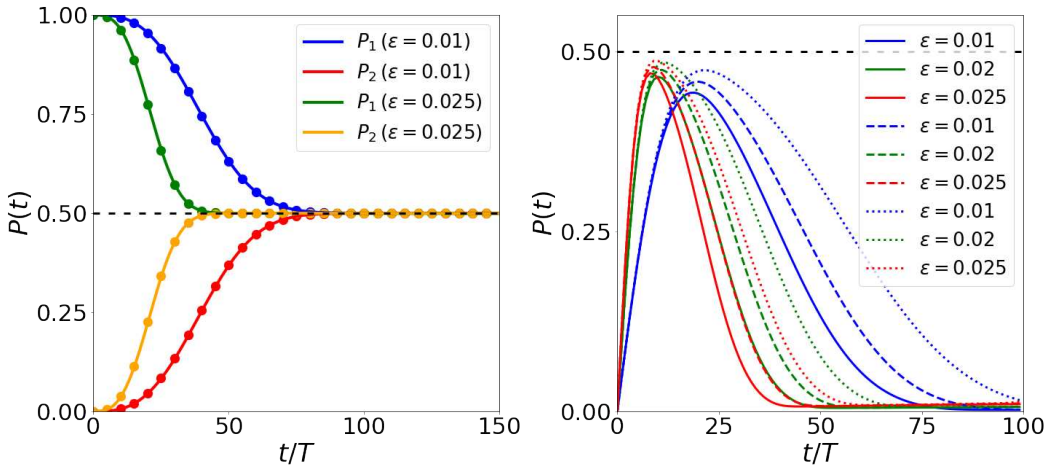

(**a**) (**b**)

Figure A1. Phonon loss analysis for the constant bias voltage: (**a**) eigenvalues of the density matrix for different values of the coupling parameter ϵ and fixed value of phonon loss rate $\Gamma_{loss}^{-1} = 100T$; P_1 (P_2) represents the probability of finding a state with the positive (negative) parity. Solid curves represent numerically obtained values while the dots represent analytical solutions from Equation (A3); (**b**) entanglement negativity for different values of ϵ (different colours) and different values of phonon loss rates: $\Gamma_{loss}^{-1} = 100T$ (solid line), $\Gamma_{loss}^{-1} = 160T$ (dashed line), $\Gamma_{loss}^{-1} = 320T$ (dotted line); T is the period of mechanical oscillations.

As can be seen, lower ϵ for a fixed Γ_{loss} means lower maximum negativity, but the peak of the negativity is wider and thus the subsystems are entangled for longer times. On the other hand, decreasing Γ_{loss} increases both the maximum value and the width of the negativity peak.

References

1. Schumacher, B. Quantum coding. *Phys. Rev. A* **1995**, *51*, 2738. [CrossRef]
2. Nielsen, M.A.; Chuang, I. *Quantum Computation and Quantum Information*; Cambridge University Press: Cambridge, UK, 2010; ISBN 978-1-107-00217-3.
3. Bergou, J.A.; Hillery, M.; Saffman, M. *Quantum Information Processing: Theory and Implementation*; Graduate Texts in Physics; Springer: Cham, Switzerland, 2021; ISBN 978-3-030-75435-8. [CrossRef]
4. Blais, A.; Girvin, S.M.; Oliver, W.D. Quantum information processing and quantum optics with circuit quantum electrodynamics. *Nat. Phys.* **2020**, *16*, 247–256. [CrossRef]
5. Martinis, J.M.; Devoret, M.H.; Clarke, J. Quantum Josephson junctions and the dawn of artificial atoms. *Nat. Phys.* **2020**, *16*, 234. [CrossRef]
6. Mirhosseini, M.; Sipahigil, A.; Kalaee, M.; Painter, O. Superconducting qubit to optical photon transduction. *Nature* **2020**, *588*, 599–603. [CrossRef]
7. Leibfried, D.; Blatt, R.; Monroe, C.; Wineland, D. Quantum dynamics of single trapped ions. *Rev. Mod. Phys.* **2003**, *75*, 281–324. [CrossRef]
8. Orlando, T.P.; Mooij, J.E.; Tian, L.; van der Wal, C.H.; Levitov, L.S.; Lloyd, S.; Mazo, J.J. Superconducting persistent-current qubit. *Phys. Rev. B* **1999**, *60*, 15398. [CrossRef]
9. Koch, J.; Yu, T.M.; Gambetta, J.; Houck, A.A.; Schuster, D.I.; Majer, J.; Blais, A.; Devoret, M.H.; Girvin, S.M.; Schoelkopf, R.J. Charge-insensitive qubit design derived from the Cooper pair box. *Phys. Rev. A* **2007**, *76*, 042319. [CrossRef]
10. Schreier, J.A.; Houck, A.A.; Koch, J.; Schuster, D.I.; Johnson, B.R.; Chow, J.M.; Gambetta, J.M.; Majer, J.; Frunzio, L.; Devoret, M.H.; et al. Suppressing charge noise decoherence in superconducting charge qubits. *Phys. Rev. B* **2008**, *77*, 180502. [CrossRef]

11. Bouchiat, V.; Vion, D.; Joyez, P.; Esteve, D.; Devoret, M.H. Quantum coherence with a single Cooper pair. *Phys. Scr.* **1998**, *T76*, 165–170. [CrossRef]
12. Nakamura, Y.; Pashkin, Y.; Tsai, J. Coherent control of macroscopic quantum states in a single-Cooper-pair box. *Nature* **1999**, *398*, 786–788. [CrossRef]
13. Matveev, K.A.; Gisselfält, M.; Glazman, L.I.; Jonson, M.; Shekhter, R.I. Parity-induced suppression of the Coulomb blockade of Josephson tunneling. *Phys. Rev. Lett.* **1993**, *70*, 2940. [CrossRef]
14. Lehnert, K.W.; Bladh, K.; Spietz, L.F.; Gunnarsson, D.; Schuster, D.I.; Delsing, P.; Schoelkopf, R.J. Measurement of the Excited-State Lifetime of a Microelectronic Circuit. *Phys. Rev. Lett.* **2003**, *90*, 027002. [CrossRef]
15. Laird, E.A.; Pei, F.; Tang, W.; Steele, G.A.; Kouwenhoven, L.P. A high quality factor carbon nanotube mechanical resonator at 39 GHz. *Nano Lett.* **2012**, *12*, 193–197. [CrossRef]
16. Tao, Y.; Boss, J.M.; Moores, B.A.; Degen, C.L. Single-crystal diamond nanomechanical resonators with quality factors exceeding one million. *Nat. Commun.* **2014**, *5*, 3638. [CrossRef]
17. Bereyhi, M.J.; Arabmoheghi, A.; Beccari, A.; Fedorov, S.A.; Huang, G.; Kippenberg, T.J.; Engelsen, N.J. Perimeter Modes of Nanomechanical Resonators Exhibit Quality Factors Exceeding 10^9 at Room Temperature. *Phys. Rev. X* **2022**, *12*, 021036. [CrossRef]
18. Bienfait, A.; Satzinger, K.J.; Zhong, Y.P.; Chang, H.-S.; Chou, M.-H.; Conner, C.R.; Dumur, É.; Grebel, J.; Peairs, G.A.; Povey, R.G.; et al. Phonon-mediated quantum state transfer and remote qubit entanglement. *Science* **2019**, *364*, 368–371. [CrossRef]
19. Satzinger, K.J.; Zhong, Y.P.; Chang, H.-S.; Peairs, G.A.; Bienfait, A.; Chou, M.-H.; Cleland, A.Y.; Conner, C.R.; Dumur, É.; Grebel, J.; et al. Quantum control of surface acoustic-wave phonons. *Nature* **2018**, *563*, 661–665. [CrossRef]
20. Vlastakis, B.; Kirchmair, G.; Leghtas, Z.; Nigg, S.E.; Frunzio, L.; Girvin, S.M.; Mirrahimi, M.; Devoret, M.H.; Schoelkopf, R.J. Deterministically Encoding Quantum Information Using 100-Photon Schrödinger Cat States. *Science* **2013**, *342*, 607–610. [CrossRef]
21. Ma, S.-L.; Li, Z.; Fang, A.-P.; Li, P.-B.; Gao, S.-Y.; Li, F.-L. Controllable generation of two-mode-entangled states in two-resonator circuit QED with a single gap-tunable superconducting qubit. *Phys. Rev. A* **2014**, *90*, 062342. [CrossRef]
22. Roy, A.; Leghtas, Z.; Stone, A.D.; Devoret, M.H.; Mirrahimi, M. Continuous generation and stabilization of mesoscopic field superposition states in a quantum circuit. *Phys. Rev. A* **2015**, *91*, 013810. [CrossRef]
23. Leghtas, Z.; Touzard, S.; Pop, I.M.; Kou, A.; Vlastakis, B.; Petrenko, A.; Sliwa, K.M.; Narla, A.; Shankar, S.; Hatridge, M.J.; et al. Confining the state of light to a quantum manifold by engineered two-photon loss. *Science* **2015**, *347*, 853–857. [CrossRef]
24. Ma, S.-L.; Xie, J.-K.; Li, F.-L. Generation of superposition coherent states of microwave fields via dissipation of a superconducting qubit with broken inversion symmetry. *Phys. Rev. A* **2019**, *99*, 022302. [CrossRef]
25. Liao, J.-Q.; Huang, J.-F.; Tian, L. Generation of macroscopic Schrödinger-cat states in qubit-oscillator systems. *Phys. Rev. A* **2016**, *93*, 033853. [CrossRef]
26. Hacker, B.; Welte, S.; Daiss, S.; Shaukat, A.; Ritter, S.; Li, L.; Rempe, G. Deterministic creation of entangled atom-light Schrödinger-cat states. *Nat. Photonics* **2019**, *13*, 110–115. [CrossRef]
27. Armour, A.D.; Blencowe, M.P.; Schwab, K.C. Entanglement and Decoherence of a Micromechanical Resonator via Coupling to a Cooper-Pair Box. *Phys. Rev. Lett.* **2002**, *88*, 148301. [CrossRef]
28. Voje, A.; Kinaret, J.M.; Isacsson, A. Generating macroscopic superposition states in nanomechanical graphene resonators. *Phys. Rev. B* **2012**, *85*, 205415. [CrossRef]
29. Xiong, B.; Li, X.; Chao, S.L.; Yang, Z.; Zhang, W.Z.; Zhou, L. Generation of entangled Schrödinger cat state of two macroscopic mirrors. *Opt. Express* **2019**, *27*, 13547–13558. [CrossRef]
30. Hou, Q.; Yang, W.; Chen, C.; Yin, Z. Generation of macroscopic Schrödinger cat state in diamond mechanical resonator. *Sci. Rep.* **2016**, *6*, 37542. [CrossRef]
31. Radić, D.; Choi, S.J.; Park, H.C.; Suh, J.; Shekhter, R.I.; Gorelik, L.Y. Nanomechanical cat states generated by a dc voltage-driven Cooper pair box qubit. *npj Quantum Inf.* **2022**, *8*, 74. [CrossRef]
32. Radić, D.; Gorelik, L.Y.; Kulinich, S.I.; Shekhter, R.I. Transduction of quantum information from charge qubit to nanomechanical cat-state. *Phys. B Condens. Matter* **2023**, *665*, 415049. [CrossRef]
33. Schneider, B.H.; Etaki, S.; van der Zant, H.S.J.; Steele, G.A. Coupling carbon nanotube mechanics to a superconducting circuit. *Sci. Rep.* **2012**, *2*, 599. [CrossRef] [PubMed]
34. Hann, C.T.; Zou, C.-L.; Zhang, Y.; Chu, Y.; Schoelkopf, R.J.; Girvin, S.M.; Jiang, L. Hardware-Efficient Quantum Random Access Memory with Hybrid Quantum Acoustic Systems. *Phys. Rev. Lett.* **2019**, *123*, 250501. [CrossRef] [PubMed]
35. Chu, Y.; Kharel, P.; Yoon, T.; Frunzio, L.; Rakich, P.T.; Schoelkopf, R.J. Creation and control of multi-phonon Fock states in a bulk acoustic wave resonator. *Nature* **2018**, *563*, 666–670. [CrossRef] [PubMed]
36. Horodecki, R.; Horodecki, P.; Horodecki, M.; Horodecki, K. Quantum entanglement. *Rev. Mod. Phys.* **2009**, *81*, 865. [CrossRef]
37. Gorelik, L.Y.; Isacsson, A.; Galperin, Y.M.; Shekhter, R.I.; Jonson, M. Coherent transfer of Cooper pairs by a movable grain. *Nature* **2001**, *411*, 454–457. [CrossRef]

38. Isacsson, A.; Gorelik, L.Y.; Shekhter, R.I.; Galperin, Y.M.; Jonson, M. Mechanical Cooper Pair Transportation as a Source of Long-Distance Superconducting Phase Coherence. *Phys. Rev. Lett.* **2002**, *89*, 277002. [CrossRef]
39. Case, W.B. Wigner functions and Weyl transforms for pedestrians. *Am. J. Phys.* **2008**, *76*, 937–946. [CrossRef]
40. See catalogues of commercially available voltage sources, e.g., Keysight B2961A manufactured by the Keysight Technologies.
41. Peng, H.B.; Chang, C.W.; Aloni, S.; Yuzvinsky, T.D.; Zettl, A. Ultrahigh Frequency Nanotube Resonators. *Phys. Rev. Lett.* **2006**, *97*, 087203. [CrossRef]
42. De Franceschi, S.; Kouwenhoven, L.; Schönenberger, C.; Wernsdorfer, W. Hybrid superconductor–quantum dot devices. *Nat. Nanotechnol.* **2010**, *5*, 703–711. [CrossRef]
43. Ming, X.; Huang, H.; Zorman, C.A.; Mehregany, M.; Roukes, M.L. Nanodevice motion at microwave frequencies. *Nature* **2003**, *421*, 496.
44. Masuda, K.; Moriyama, S.; Morita, Y.; Komatsu, K.; Takagi, T.; Hashimoto, T.; Miki, N.; Tanabe, T.; Maki, H. Thermal and quantum phase slips in niobium-nitride nanowires based on suspended carbon nanotubes. *Appl. Phys. Lett.* **2016**, *108*, 222601. [CrossRef]
45. Eriksson, A.M.; Vikström, A. Zero-Phase-Difference Josephson Current Based on Spontaneous Symmetry Breaking via Parametric Excitation of a Movable Superconducting Dot. *Phys. Rev. Lett.* **2017**, *118*, 197701. [CrossRef] [PubMed]
46. Amico, L.; Fazio, R.; Osterloh, A.; Vedral, V. Entanglement in many-body systems. *Rev. Mod. Phys.* **2008**, *80*, 517–576. [CrossRef]
47. Radić, D.; Gorelik, L.Y.; Kulinich, S.I.; Shekhter, R.I. Nanomechanical manipulation of superconducting charge-qubit quantum networks. *Phys. B Condens. Matter* **2024**, *684*, 415988. [CrossRef]